Investigation of the Mechanical Behavior of Microbeam-Based MEMS Devices

Mohammad I. Younis

Thesis submitted to the Faculty of the
Virginia Polytechnic Institute and State University
in partial fulfillment of the requirements for the degree of

Master of Science
in
Engineering Mechanics

Ali H. Nayfeh, Chairman
Dean T. Mook
Scott L. Hendricks

December 13, 2001
Blacksburg, Virginia

Keywords: MEMS, Reduced-Order Model, Electrostatic Resonators, Capacitive Microswitches, Pull-in

Investigation of the Mechanical Behavior of Microbeam-Based MEMS Devices

Mohammad I. Younis

(ABSTRACT)

An investigation into the responses of microbeams to electric actuations is presented. Attention is focused mainly on the use of microbeams in two important MEMS-based devices: capacitive microswitches and resonant microsensors. Nonlinear models are developed to simulate the behavior of the microbeams in each device. The models account for mid-plane stretching, an applied axial load, a DC electrostatic force, and, for the case of resonant sensors, an AC harmonic force. Further, a novel method that uses a reduced-order model is introduced for simulating the behavior of microbeams under a DC electrostatic force. The presented method shows attractive features, like for example, a high stability near the pull-in and a low computational cost. Thus, it can be of significant benefit to the development of MEMS design software.

The static behavior of microbeams under electrostatic forces is studied using two methods. One method employs a shooting technique for solving the boundary-value problem that governs the static behavior. The second method is based on solving an algebraic system of equations obtained from the reduced-order model. Further, the eigenvalue problem describing the vibrations of a microbeam around its statically deflected position is solved using a shooting method to obtain the microbeam mode shapes and natural frequencies. The dynamic behavior of resonant microbeams is also investigated. A perturbation method, the method of multiple scales, is used to obtain two first-order nonlinear ordinary-differential equations that describe the amplitude and phase of the response and its stability. The results show that an inaccurate representation of the system nonlinearities may lead to an erroneous prediction of the nonlinear resonance frequency of a microbeam. The case of three-to-one internal resonance between the lowest two modes is treated. Finally, the reduced-order model is used to study the dynamic behavior of the electrostatically actuated microbeams.

The proposed models are validated by comparing their results with experimental results available in the literature.

Dedication

To my Father, Mother, and Wife

Acknowledgments

I would like to express my sincere gratitude and deep appreciation to my advisor Dr. Ali Nayfeh. His patience, encouragement, and endless support are deeply acknowledged. His ingenuity, distinguished supervision, and insightful guidance are greatly admired. His kind character was a great source of inspiration to me. It has been a great honor and pleasure for me to be his student.

I would like to thank my committee members Drs. Dean Mook and Scott Hendricks for their support and trust. I would like to thank Dr. Eihab Abdel-Rahman who collaborated with me in some of the work in this thesis. His insightful thoughts and deep discussions were of a great benefit to me. Also, I would like to thank Dr. Haider Arafat for his invaluable discussions and comments while conducting my research. I am deeply thankful to him for valuable additions and suggestions on the thesis. I would like to thank the people and friends of the Nonlinear Dynamics Group. In particular, I would like to thank Dr. Osama Ashour for helping me a lot with the new life in Blacksburg and for supporting me while pursuing my study, and also Mr. Waleed Faris for his valuable advice and help. Words of thanks go to my dearest friends Mohammad Sha'aban and Mohmmad Abo-Zakyah for their belief in me and for being very supportive in all of my life stages.

I would like to express my deep thanks and appreciation to my parents for supporting me all over the years by their patience, sacrifice, and prayers for me to succeed. Their continuous encouragement and close follow and care have been the forces that have kept me strong and determined to achieve my goals. Thanks are due to my sister who has been beside me all the time. Also, I would like to thank my youngest brother

Hani for doing so much to help me and with whom I share so many nice memories and exciting moments. Finally, many thanks go to my wife for her support, understanding, and belief in me. I am forever grateful for her kindness and love.

Contents

1 Introduction **1**

1.1 Background and Motivation 1

1.2 Literature Review 4

1.2.1 Resonant Sensors 4

1.2.2 Capacitive Microswitches 7

1.3 Contributions of the Thesis 11

1.4 Thesis Objectives and Organization 12

2 Introduction to Electrostatic MEMS **15**

2.1 Electrically Actuated Resonant Sensors 15

2.2 Capacitive Microswitches 17

3 Problem Formulations **20**

3.1 Resonant Sensors Model 20

3.2 Capacitive Microswitch Models 25

3.2.1 Continuous System Model 25

3.2.2 Reduced-Order Models (Macromodels) 25

4 Static Response of Microbeams to a DC Electrostatic Force **29**

4.1 A Shooting Method for Solving the Static Boundary-Value Problem . . 29

4.1.1 Numerical Scheme 29

4.1.2 Effect of the Nondimensional Design Parameters on the Static Behavior 31

4.2 Reduced-Order Models for Simulating the Microbeams Static Behavior 34

5 Natural Frequencies and Mode Shapes of Microbeams under a DC Electrostatic Force 42

5.1 Numerical Results 42

5.2 Discussion 45

6 Nonlinear Response of Microbeams to a Combined DC and AC Electric Force 48

6.1 Primary Resonance of the First Mode 49

6.1.1 Perturbation Analysis 49

6.1.2 Results 55

6.1.3 Discussion 60

6.2 Three-to-one Internal Resonance 63

6.2.1 Perturbation Analysis 63

6.2.2 Results 67

7 Dynamic Behavior of Microbeams under a DC Electrostatic Force 69

8 Concluding Remarks and Recommendations 74

8.1 Summary 74

8.1.1 Static Behavior and Natural Frequencies of Microbeams under a DC Electrostatic Force 74

8.1.2 Nonlinear Response of Microbeams to an Electric Actuation . . . 75

8.1.3 Reduced-Order Models of Microbeams 77

8.2 Recommendations for Future Work 78

List of Figures

3.1 A schematic drawing of a resonant microbeam. 21

4.1 Variation of the maximum nondimensional deflection W_{Max} with $\alpha_2 V_p^2$ for α_1 of 0.1, 1.0, 10.0, 20.0, 25.0, and 30.0 and no axial load. 31

4.2 Comparison of the maximum deflection W_{Max} calculated using our model (solid line) with that calculated by Choi and Lovell [5] (circles) for $\alpha_1 = 1.5$ and $N = 0$. 32

4.3 Variation of the maximum nondimensional deflection W_{Max} with $\alpha_2 V_p^2$ when $\alpha_1 = 3.7$ for various axial forces. 33

4.4 Variation of the level of electrostatic forcing, represented by $\alpha_2 V_p^2$, at pull-in with the axial force for $\alpha_1 = 0.1, 3.7$ and 10.0. 34

4.5 Comparison of the calculated maximum nondimensional deflection W_{Max} (dashed line) using a three-symmetric-mode discretized system of equations, equations 4.2, with that obtained by solving the static boundary-value problem using a shooting method (solid lines) for various values of V_p. The electrostatic force term $\frac{1}{(1-w)^2}$ was expanded using a Taylor series around w=0 up to fifth order 36

4.6 The influence of the number of symmetric modes retained in the discretization on the variation of u_1 with V_p. 37

4.7 Variation of W_{Max} calculated with the second discretization method using linear symmetric modes for two cases: the first uses the first three modes (dashed line) and the second uses the first five modes (solid line). The two curves are compared with results obtained by solving the boundary-value problem using a shooting method (diamonds). . . . 38

4.8 Variations of W_{Max} calculated using the second discretization method for various values of V_p and α_1=50, α_2=3.904, and no axial load. The dashed line denotes an unstable solution and the solid line denotes a stable solution. 40

5.1 Comparison of the normalized fundamental natural frequency calculated using our model (solid lines) with those obtained theoretically (dashed lines) and experimentally by Tilmans and Legtenberg [7] for a $210\mu m$ length microbeam (circles) and for a $510\mu m$ length microbeam (diamonds). 43

5.2 Variation of the fundamental natural frequency with $\alpha_2 V_p^2$ for various values of α_1 and no axial load. 44

5.3 Variation of the fundamental natural frequency with $\alpha_2 V_p^2$ when $\alpha_1 =$ 3.7 for various axial forces. 45

5.4 Variation of the first four natural frequencies of the microbeam with $\alpha_2 V_p^2$ for various values of α_1 and no axial load. 46

5.5 Variation of the first four natural frequencies with $\alpha_2 V_p^2$ for $\alpha_1 = 3.7$ and various applied axial loads. 47

6.1 Comparison of the normalized nonlinear resonance frequency $\frac{\Omega_r}{\omega}$ calculated using our model (solid lines) with those obtained theoretically (dashed lines) and experimentally by Tilmans and Legtenburg [7] for two microbeams of lengths $210\mu m$ (diamonds) and $310\mu m$ (circles). The thin solid lines are based on the quality factors of Tilmans and Legtenburg [7] and the thick solid lines are based on quality factors estimated using our model. 56

6.2 Comparison of the hysteretic points obtained using our model (solid lines) with those obtained theoretically (dashed line) and experimentally (circles) by Gui et al. [10]. The thin solid line is based on the quality factor $Q = 900$ reported by Gui et al. and the thick solid line is based on a quality factor $Q = 1000$ estimated using our model. 57

6.3 Variation of the normalized nonlinear resonance frequency $\frac{\Omega_r}{\omega}$ with V_{AC} for various values of the nondimensional axial load N. The values of α_1, $\alpha_2 V_p^2$, and Q are 3.7, 5.5, and 796, respectively. 58

6.4 Variation of the normalized nonlinear resonance frequency $\frac{\Omega_r}{\omega}$ with V_{AC} for various values of α_1. The values of N, $\alpha_2 V_p^2$, and Q are 8.7, 5.5, and 796, respectively. 59

6.5 Variation of the normalized nonlinear resonance frequency $\frac{\Omega_r}{\omega}$ with V_{AC} for various values of $\alpha_2 V_p^2$. The values of α_1, N, and Q are 3.7, 8.7, and 796, respectively. 60

6.6 Variation of the nonlinear coefficients with the axial load N. The values of α_1 and $\alpha_2 V_p^2$ are 3.7 and 5.5, respectively. 61

6.7 Variation of the nonlinear coefficients with α_1. The values of N and $\alpha_2 V_p^2$ are 8.7 and 5.5, respectively. 62

6.8 Variation of the nonlinear coefficients with $\alpha_2 V_p^2$. The values of α_1 and N are 3.7 and 8.7, respectively. 63

7.1 Evolution of u_1 with the nondimensional time showing the onset of pull-in. The results are obtained using a nondimensional damping coefficient c =260 and a DC voltage V_p=10 V. 70

7.2 Comparison of the pull-in time obtained using the first three symmetric modes (dashed line) with that obtained using the first five symmetric modes (solid line) for various values of V_p and c =260. 71

7.3 Comparison of the pull-in time t_p obtained using our model (solid lines) with those obtained theoretically (squares) and experimentally (triangles) by Hung and Senturia [22]. The thin solid line is based on the a nondimensional damping coefficient c =160 estimated by Gupta and Senturia [35] for the same device in [22] and the thick solid line is based on the nondimensional damping coefficient c =260 estimated using our model. 72

Chapter 1

Introduction

1.1 Background and Motivation

The area of microelectromechanical systems (MEMS) first gained attention in the late 1960's when IBM and Westinghouse demonstrated the first silicon-based MEMS [1]. The actual interest in MEMS, however, did not start until two decades later when micromachining technology revolutionized the industry with novel manufacturing techniques, making it possible to fabricate tiny devices in the micro scale with very high precision.

MEMS promise attractive features over other conventional devices. The main advantages include small size and light weight; inexpensive operation and low-power consumption; compatibility with integrated circuit (IC) processes, which allows fabricating thousands of MEMS devices on a single wafer at a greatly reduced cost; and the ability to place electronic components directly on MEMS devices without the need for any cumbersome electrical components, which reduces electrical noise and improves precision and sensitivity. As a result, considerable attention is being focused on the development of MEMS and their implementation into new applications. So far, few MEMS devices have seen the light in industrial applications. Successful examples are accelerometers in automobile airbags, micropressure transducers, and micromirror arrays for image projection. Nevertheless, there are many other devices, especially in the microsensing and microactuating technology, that are currently under extensive

research and are expected to be in market within the next few years.

Because of their small size and light weight, MEMS actuation methods demand very low power. These include thermal, magnetic, piezoelectric, hydraulic, and electric actuations. Among them, electric actuation is the most common and well-developed method. Electric actuation may use either strictly DC voltages, in which case it is referred to as electrostatic actuation, or a combination of AC and DC voltages. It offers high energy density, high mechanical flexibility, and well-controlled force over several microns of displacement, and requires very low current. In this method, the driving load is simply the attractive force between two electrodes of a capacitor. This force drives a mechanical element, like a beam or a plate, to serve different functions, such as to oscillate at resonance, as in resonant sensors, or to move back and forth, as in switches, to transmit signals in electronic circuits.

Electrically actuated microbeams form the heart of a wide class of MEMS-based devices, which include resonant sensors, capacitive switches, pull-in sensors, and electrostatic actuators. The present work focuses on the first two devices. In resonant sensors, a microbeam is deflected by an electrostatic force and then is driven to oscillate at resonance around the deflected position by an AC electric force. On the other hand, in capacitive microswitches, a microbeam carrying a contact bar is actuated by an electrostatic force to close or open an electric circuit.

Many approaches have been proposed to simulate the behavior of microbeams in resonant sensors and capacitive microswitches. In many cases, a lumped spring-mass system is used, thereby neglecting the mass distribution of the microbeam. In other cases, generic softwares based on finite-element methods (FEM) are used, which are not designed to address cases involving nonlinear electric forces or large deflections of mechanical elements. On the other hand, some researchers have developed computer-aided design softwares especially designed for electromechanical systems. These programs utilize FEM, which use numerous variables to represent the device state. Thus, these programs have the shortcomings of being complex and expensive and requiring huge computational cost. Moreover, they complicate the feedback control of the device.

Most of the proposed models in the literature neglect or misrepresent much of the

nonlinearities that exist in electrostatic MEMS devices. Parallel-plate electric forces are inherently nonlinear because they are inversely proportional to the square of the distance between the capacitor plates. Thus, linearizing these forces, as many models in the literature do, restricts the analysis to small values of DC and AC voltages. These electric forces can produce large deflections when acting on micro-scale components, where linear theories do not apply. Moreover, large deflections introduce geometric nonlinearities, such as mid-plane stretching in beams of immovable ends. Mid-plane stretching tends to shift the natural frequencies of microbeams to higher values, whereas a DC electrostatic force tends to shift the natural frequencies to lower values.

Electric forces introduce a new instability concept called 'Pull-in.' This phenomenon occurs when the mechanical restoring force of a microbeam can no longer resist the opposing electric forces, thereby leading to a continuous increase in the microbeam deflection and, accordingly, an increase in the electric forces in a positive feedback loop. This behavior continues until a physical contact is made with the stationary electrode. It has been shown that linear modeling and analysis underestimate the location of this instability [2].

It is well-known that linear modeling and analysis are generally inadequate to fully capture the dynamics of structures having nonlinearities, and even can be misleading in predicting their mechanical behavior [3]. Thus, a model that accounts for the nonlinearities of the system becomes necessary for successful simulation, especially when studying electrically actuated MEMS.

In the present work, we study electrically actuated microbeams in capacitive microsensors and microswitches using models that account for their nonlinearities, and also introduce novel techniques for simulating MEMS devices using reduced-order models for efficient, accurate, and fast simulation.

1.2 Literature Review

1.2.1 Resonant Sensors

Several studies have investigated the behavior of electrically actuated microbeams in resonant microsensors. These studies fall under two categories. The first category focuses on the static behavior of microbeams when deflected by a DC electrostatic force and the effect of this force on their natural frequencies and modes shapes. The second category focuses on the vibrations of microbeams around the deflected position due to an AC harmonic force.

To begin with, we list contributions of the first group. Tilmans et al. [4] studied the response of a microbeam to a general transverse excitation and subject to an axial force. They used Rayleigh's energy method to approximate the fundamental natural frequency of a straight, undeflected microbeam. To account for mid-plane stretching, they added an additional term to the frequency expression. However, the added term is incorrect, as we show in Appendix A. Also, the model does not apply to electric actuation because it assumes that the transverse load is independent of the microbeam deflection.

Zook et al. [5] assumed both a beam model and a plate model and used a finite element method to calculate the natural frequencies of a microbeam driven at resonance by an electric force and subject to an axial load. They also determined experimentally the natural frequencies of the microbeam. The finite element models accounted for shear deformation and rotary inertia, but neglected the effect of the DC force. Their calculations showed no significant differences between the natural frequencies produced by the beam and plate models. However, the calculated natural frequencies were consistently higher than those measured experimentally. That is probably due to the fact that their model does not include the effect of the DC force.

Ijntema and Tilmans [6] considered the static and dynamic responses of a microbeam under an electric actuation, but did not account for the mid-plane stretching. They calculated the static deflection due to an electrostatic force applied by a DC polarization voltage. The fundamental natural frequency was then approximated us-

ing Rayleigh's energy method, where the microbeam motion was linearized around the deflected shape obtained as a solution of the static problem. Tilmans and Legtenberg [7] solved the same static problem by using the Rayleigh-Ritz method and assuming a single admissible trial function. They used this formulation to generate an analytical expression for the pull-in voltage. Their calculated values for the pull-in voltage were in good agreement with experiments they had conducted on resonators of various lengths. They compared the approximation of the fundamental frequency obtained from Rayleigh's energy method with that obtained experimentally. They found out that the results obtained from Rayleigh's energy method were only valid for small DC polarization voltages away from the pull-in voltage.

Choi and Lovell [8] numerically calculated the static deflection of a microbeam using a shooting method. Their model accounts for both the electrostatic force and mid-plane stretching.

Ahn et al. [9] modeled a microbeam under an electrostatic actuation as a single-degree-of-freedom spring-mass-damper system. The model assumed a linear spring, thus neglected mid-plane stretching. They used this model to generate an analytical expression for the fundamental natural frequency as a function of the DC polarization voltage. Both of this expression and the experiments they carried on a resonator showed that increasing the DC polarization voltage decreases the fundamental natural frequency.

In the second group of researches, we begin with Zook et al. [5] who reported experimentally that increasing the driving AC voltage leads to an increase in the resonance frequency (hardening behavior). Also, they observed a hysteresis that depends on the direction of the frequency sweep.

Tilmans and Legtenberg [7] approximated the fundamental natural frequency as the nonlinear resonance frequency for small values of the AC forcing amplitude. For large-amplitude AC excitations, they approximated the dynamic problem using Rayleigh's energy method, modified to account for electric forces and mid-plane stretching. However, mid-plane stretching, as we show in Appendix A, was misrepresented. They derived an equation that governs the resonance frequency as a function of the excitation

amplitude. They compared the results obtained using this equation to experimental results. Although they found a good qualitative agreement, showing a hardening effect, the agreement was poor quantitatively. They concluded that such a hardening behavior is more severe for high quality factors, high DC voltages, and high AC voltages, whereas large axial strains can decrease it.

Gui et al. [10] investigated the dynamic problem using Rayleigh's energy method, modified to account for electric forces and mid-plane stretching, which was misrepresented as in [7]. They neglected the applied axial force. They derived an equation for the fundamental resonance frequency, which predicts a hardening behavior. They also derived a criterion that defines a region of DC and AC voltages for a hysteresis-free operation. They compared their theoretical and experimental results and found good agreement.

Turner and Andrews [11] approximated the fundamental natural frequency of a microbeam as the nonlinear resonance frequency. The problem was modeled using a spring-mass system with a cubic nonlinearity representing the mid-plane stretching, but they neglected the AC force. Using the method of harmonic balance, they derived equations describing the microbeam resonance frequency for two separate cases. In one case, they neglected the electrostatic force and included mid-plane stretching, and, in the second case, they included the electrostatic force and neglected mid-plane stretching. Using the equations obtained from both cases, they derived an equation that compensates for the increase in the resonance frequency due to mid-plane stretching and the decrease in the resonance frequency caused by the electrostatic force. The results showed that eliminating the effect of the frequency dependence on the amplitude requires a very high DC voltage, which may not be attainable.

Ayela and Fournier [12] experimentally studied the response of microbeams of different geometric shapes to a general electric load composed of DC and AC components. They made several plots to show the variation of the resonance frequency with the excitation amplitude for different axial loads. The experimental data were used to extract parameters that fit the equation of a spring-mass system with cubic nonlinearity and linear electric force (i.e., the electric force is assumed to be independent of

the gap distance). The experimental results showed that, for the operating conditions used, some devices exhibited softening behavior, whereas others exhibited hardening behavior. They concluded that a nonlinear behavior may result from many distinct phenomena and that each case has to be studied separately. They added that the nonlinear behavior of these devices may be investigated experimentally, but there is no way of predicting it analytically.

Veijola et al. [13] modeled a microbeam using a spring-mass model with a cubic nonlinearity representing the mid-plane stretching. They included the effect of the driving AC voltages, but neglected the effect of the DC polarization voltages. They used the method of harmonic balance to show that the nonlinearity of the electrostatic forces can cause a softening-type behavior, whereas the mid-plane stretching can cause a hardening-type behavior. They conducted an experiment, which showed a hardening behavior. They used the results to extract values for the parameters involved in their model. They compared the experimental results with those obtained using their model and found them to be in good agreement. However, they did not give an explanation for observing a hardening rather than a softening behavior.

1.2.2 Capacitive Microswitches

The static behavior of a microbeam in capacitive microswitches is governed by the same static equations in resonant sensors because, in either case, a microbeam is deflected by a constant DC force. However, the principle of operation and the dynamic behavior are different in microswitches. We present details of these differences in Chapter 2 when we introduce electrostatic MEMS.

The behavior of electrostatically actuated microbeams in capacitive microswitches has been studied using different models and approaches. We can identify two groups of studies that are presented on this topic. The first group focuses on manufacturing techniques, introducing new designs, and testing the performance of proposed devices. Simple models are used to predict the mechanical behavior. In some cases, the device is simulated using finite element softwares, even though they are not designed to treat problems involving electrostatic forces or large deflections of microbeams. The second

group, on the other hand, gives more attention to modeling the devices and predicting their behaviors rather than to building and testing them. Toward this purpose, considerable efforts have been done to develop computational methods and computer-aided programs to enable designers to simulate their devices by inexpensive computer simulations instead of conducting expensive experimental tests.

We begin by summarizing contributions of the first group from selected typical papers. All microbeams mentioned in the review are assumed to be actuated by a constant DC electrostatic force. Zavracky et al. [14] built a micromechanical switch with a cantilever microbeam as the switching element. They presented a model to study the microbeam static behavior assuming no applied axial load. They calculated the microbeam deflection at various DC voltages by numerically solving the fourth-order static equation. They used a spring-mass model to derive equations to describe the maximum deflection and to predict the pull-in voltage. Using these equations, they showed that two solutions exist at each DC voltage, and that both solutions coalesce at the pull-in voltage. They concluded that one of them is unstable since it gives a maximum deflection beyond the size of the airgap. They compared the results obtained numerically with those obtained using the derived equations. They concluded that the spring-mass model is inaccurate since it predicts the pull-in voltage at a maximum deflection near one-third the gap, while the numerical solution predicts a higher value. Thus, they modified the derived equations to fit the numerical results.

Chan et al. [15] studied the static behavior of a fixed-fixed microbeam. They created a 2-D mechanical model using the finite element package ABAQUS. Residual stresses were included in the model, but mid-plane stretching was not. They compared the computed maximum deflections using their model with those obtained by using the finite element programs 3-D IntelliCAD and Quasi 2-D. The Quasi 2-D simulator model included the effects of mid-plane stretching. The results of all three programs were in good agreement. They indicated that the 3-D simulations took much more time compared with the other methods and that the observed out-of-plane bending was very small. They calculated the pull-in voltages using ABAQUS for microbeams of different lengths and compared the results with experimental results.

Grtétillat et al. [16] presented a new design for a microswitch using a fixed-fixed microbeam and studied experimentally its characterization. They tested the device and reported its pull-in voltage, switching time, fundamental natural frequency, and the maximum working frequency. They concluded that the maximum working frequency of a microbeam is approximately equal to one-third its fundamental natural frequency.

Yao et al. [17] designed and fabricated a capacitive microwave switch utilizing a fixed-fixed microbeam as the switching element. They used a spring-mass model to derive an equation that predicts the pull-in voltage. They indicated that this equation gives only a first-order approximation and hence cannot yield accurate results. They improved the results by a 3-D numerical simulation using the finite element software IntelliCAD. They compared the theoretical results with experimental results and found good agreement. They approximated the switching speed of these devices as one-fourth the period of the fundamental natural frequency. They also used ABAQUS for determining the natural frequencies of the microbeam.

In the second group of contributions, Senturia et al. [18] developed computer-aided design systems MEMCAD that can be used to simulate electrostatic MEMS. Commercial software packages were linked in the MEMCAD to allow mechanical and electrical analysis of structures. The mechanical analysis is performed using ABAQUS, while the electrostatic force is computed using the boundary-element based program FASTCAP. They proposed a scheme for determining the deflection of a microbeam actuated by a DC electrostatic force. It starts by computing the electrostatic force at the undeflected position, which is then used to deform the microbeam. Then, the electrostatic force on the deformed shape is recomputed and used to re-deform the structure, and so forth.

Gilbert et al. [19] used the 3-D electromechanical solver CoSolve-EM, which is a software that combines the electrical and mechanical analysis illustrated in [18], to predict the pull-in voltage. It is based on calculating the microbeam deflections, starting from a zero voltage and then with increasing steps until the deflection reaches a large value, where the solution starts to diverge. At that point, the displacement is then set equal to zero and the corresponding voltage is considered the pull-in voltage.

Grtétillat et al. [20] simulated the electromechanical behavior of asymmetric fixed-fixed microbeams using finite element softwares and a reduced-order model based on discretizing the equations of motion (a macromodel). They simulated the pull-in voltages using the MEMCAD system [18], the resonance frequencies of undeflected microbeams using ABAQUS, and the dynamic motion using the macromodel. The calculated pull-in voltages and resonance frequencies were compared to experimental results and were found to be in good agreement. They also calculated the pull-in time, the time that an undeflected microbeam takes to reach pull-in, for various actuation voltages and found good agreement with experimental results. The parameters involved in the macromodel were adjusted to fit the experimental pull-in voltage by either adjusting the stiffness of the microbeam or by adding external axial loads. This probably was to account for the effect of mid-plane stretching, which they neglected in the model.

Castañer and Senturia [21] used a linear spring-mass-damper system to model a parallel-plate electrostatic actuator. The axial load and mid-plane stretching were not included in the model. They studied the dynamic behavior of the plate under the electrostatic actuation and simulated the time histories of the plate displacement and velocity.

Hung and Senturia [22] used a macromodel to simulate the dynamics of a fixed-fixed microbeam proposed as a pressure sensor. They solved two coupled partial-differential equations (PDE): the first describes the microbeam behavior under the electrostatic force in the presence of damping, and the second relates the damping to the pressure and the microbeam deflection. They assumed an applied axial load to the microbeam to match the experimental pull-in voltage. They generated a macromodel by discretizing the original PDE's using the Galerkin method. They generated the global basis functions using data produced from a few runs of a fully meshed and slow finite-difference method. They indicated that the produced basis functions are similar to the linear mode shapes of the undeflected microbeam. They then computed the pull-in time using two models: the first assumes a linear damping, in which the damping coefficient is obtained by matching the experimental pull-in time to the theoretical

one, and solves the equation that governs the microbeam motion, and the second solves the coupled PDE's, which relate the damping to the motion. The results of the two models were then compared to experimental results and results obtained from a full slow finite-difference simulation. The model based on the linear damping gave poor results, whereas the results of the coupled-system model were in good agreement with the finite-difference and experimental results.

Gabbay et al. [23] developed an automated procedure for generating a macromodel from a 3D finite-element method simulation. The procedure however does not apply to nonconservative problems or to problems involving large displacements because the mid-plane stretching effect was neglected. Their method is based on using the linear mode shapes of a microbeam as basis functions. The electrostatic forces are represented by fitting a rational function of multivariate polynomials to data produced from a 3D finite-element method. They reported that the linear mode shapes fail to correctly predict the dynamics of a clamped-clamped microbeam at a DC voltage near 30% of the pull-in voltage.

Mehner et al. [24] modified the procedure of Gabbay et al. [23] to address problems involving mid-plane stretching. Thus, their modified model cannot be used for problems involving small deflections. They modified the constraints on the mesh elements of the finite-element program to stretch as they bend in a specific way that ensures not to overestimate the stiffness. In other words, they modified the data, which are used to extract the basis functions, to include the effect of mid-plane stretching. The extracted basis functions were close to, but different from, the linear mode shapes of the undeflected microbeams. The procedure was not automated and does not apply to damped systems.

1.3 Contributions of the Thesis

The contributions of this thesis are summarized as follows:

- A complete theoretical framework is presented to enable an accurate simulation of the mechanical behavior of microbeams in two MEMS-based devices: capacitive

microswitches and electrostatic resonant sensors. Comprehensive models are derived accounting for the nonlinearities of these systems due to electric forces and the geometry of a deflected microbeam of fixed ends. Design parameters are included in the models by lumping them into nondimensional parameters, thereby allowing easier understanding for their effects and for the interaction between the mechanical and electrical energies.

- Several methods are discussed to attack the nonlinear equations of the developed models. Numerical methods are introduced to simulate the static behavior and the free vibrations of microbeams under DC forces. The method of multiple scales is directly applied to predict the nonlinear response of microbeams to AC and DC electric loads. We show a successful and efficient implementation for the method of multiple scales in treating nonclassical problems having nonlinear electric forces.

- A complete study of the static and dynamic behaviors of microbeams in the two devices is presented. The results help to explain many of the phenomena reported in the literature. Also, they allow designers to tune the devices for wider operation ranges and optimum performance.

- A novel method for generating reduced-order models for MEMS devices are introduced. The new method is simple, fast, inexpensive, and accurate because it simulates the behavior of devices without the need to run large packages based on finite-element or finite-difference methods, as it is the case in the literature.

1.4 Thesis Objectives and Organization

The objective of the present work is to investigate the mechanical behavior of electrically actuated microbeams in two important MEMS-based devices. The first is resonant sensors, in which a microbeam is deflected by a DC electrostatic force and driven at resonance around the deflected position by an AC harmonic force. The second is capacitive microswitches, in which a microbeam is actuated by DC electrostatic forces.

A second objective of this work is to introduce novel techniques and methodologies for simulating electrostatic MEMS devices. These methods are based on reduced-order models and can be of significant benefit to the development of MEMS design software.

In Chapter 2, we give a brief description of each device, its principle of operation, main advantages and limitations, and other issues important to the modeling and analysis.

In Chapter 3, we formulate the problems describing the behavior of microbeams in each device and derive reduced-order models for simulating the mechanical behavior of microbeams under electrostatic actuation. We derive the equations that govern their static deflection, natural frequencies and mode shapes, and dynamic response. Then, we derive the equations that govern the dynamics of microbeams actuated by a combination of DC and AC electric forces. Finally, we propose to simulate electrostatically actuated microbeams based on the discretization of the equations of motions by using the Galerkin procedure. We present two approaches to treat the electrostatic force term in the discretization. We show in the next Chapter that only one of them predicts correct behaviors.

In Chapter 4, we study the static behavior of a microbeam under an electrostatic force. We discuss various methods for treating the problem. One method employs a shooting method for solving the boundary-value problem that governs the static behavior. The other methods are based on solving algebraic systems of equations of a reduced-order model obtained from the discretized system derived in Chapter 3. We compare these methods and draw conclusions.

In Chapter 5, we solve the eigenvalue problem describing the vibrations of a microbeam around its statically deflected position. We solve the problem numerically using a shooting method and obtain the microbeam mode shapes and natural frequencies. We validate our results by comparing with experimental results available in the literature.

In Chapter 6, we study the forced vibrations of a microbeam in resonant sensors. We apply a perturbation method, the method of multiple scales, directly to the governing integral-partial-differential equation and associated boundary conditions to ob-

tain an approximation for the microbeam response to a primary resonance excitation. Based on the perturbation analysis, we derive equations that describe the nonlinear resonance frequency, the amplitude of the periodic solution, and the stability of this solution. We study the effect of design parameters on the nonlinear resonance frequency and the effective nonlinearity of the system. We compare our results with experimental results available in the literature. Then, we investigate the possibility of activating a three-to-one internal resonance between the first and second modes.

In Chapter 7, we use the reduced-order model derived in Chapter 3 to study the dynamic behavior of microbeams and compute the time a straight microbeam takes to reach pull-in. We validate the proposed method by comparing our theoretical results with experimental results available in the literature.

Finally in Chapter 8, we present our conclusions and recommendations for future work.

Chapter 2

Introduction to Electrostatic MEMS

2.1 Electrically Actuated Resonant Sensors

Resonant sensors have been a subject of technology development in recent years. They offer attractive advantages over other conventional sensors, such as high sensitivity and resolution, low-power consumption, direct digital output (without A/D conversion), and long-term stability. Further, silicon material, which is the material resonant sensors are composed of, has other advantages, such as excellent mechanical properties, the ability to batch process at low cost, and the compatibility of mechanical and electrical components. Also, silicon possesses excellent dynamic and temperature characteristics, which are better than those of piezoresistive sensors [25].

Resonant microbeams, also referred to as resonators, act as transducers in resonant sensors. Their fundamental natural frequencies are very sensitive to axial strain. External loads, such as pressure, temperature, force, and acceleration, apply axial strains on microbeams, leading to shifts in their natural frequencies. These frequency shifts are readily converted to digital signals, which are related to the physical quantity being measured.

Various actuation methods are used to excite microbeams, such as thermal, electromagnetic, and electric excitations. We study here electric excitation because it is

the most promising and reliable method. In this method, the electric load applied to a microbeam is composed of a DC polarization voltage and an AC voltage, which is usually much smaller than the DC voltage. The addition of the DC component prevents driving the microbeam at twice the AC-forcing frequency. This is undesirable because half-frequency elements have to be introduced in the oscillator circuit to maintain driving the microbeam at resonance. These elements are expensive and complicate the structure of devices.

The structure of electrically actuated resonant sensors is made up mainly of an airgap capacitor, in which an actuated microbeam forms one of its sides, while the other side is kept stationary. Due to the oscillations of the microbeam, the capacitance of the air-gap changes, thereby inducing an AC current that is used to detect the microbeam motion. Typically, the microbeam is placed inside a sealed vacuum cavity made of silicon. The vacuum housing provides isolation from environmental effects, such as dust and vapor, which disturb the microbeam motion. It also improves the quality factor for better resolution and stable operation. The housing is exposed to the external effect to be detected and, at the same time, is integrated with the boundaries of the resonating microbeam. Thus, the microbeam and the surrounding shell is considered as the resonant sensor. The microbeam is typically heated prior to clamping its sides. When cooled, an internal axial tension is induced. This axial tension is known in the literature as residual stresses. Such stresses are desirable to minimize the possibility of buckling [27].

The electric load and the mechanical restoring force govern the behavior of the microbeam. The DC component applies an electrostatic force on the microbeam, thereby deflecting it to a new equilibrium position, while the AC component vibrates the microbeam around this equilibrium position. The combined electric load has an upper limit beyond which the mechanical restoring force can no longer resist its opposing force, thereby leading to the collapse of the microbeam. This structural instability phenomenon is known as 'pull-in,' and the critical voltage associated with it is called the 'pull-in voltage.' The microbeam restoring force is composed of two components: the beam resistance to bending and mid-plane stretching due to immovable boundaries.

The mechanical restoring force tends to shift the natural frequencies to higher values, while the electrostatic force tends to shift the natural frequencies to smaller values. Further the geometry of the deflected microbeam may lead to either a softening or a hardening behaviors, depending on whether the electric force dominates mid-plane stretching or not.

The static behavior and the pull-in phenomenon are discussed in Chapter 3. The dynamic behavior of the resonator is treated in Chapters 4 and 5.

2.2 Capacitive Microswitches

Capacitive microswitches are receiving a great deal of attention in the MEMS community because of the attractive features that characterize these devices, which open the gate for replacing conventional switches in significant market areas. Beside the common known advantages of MEMS and electrostatic actuation, capacitive switches have other important advantages in the radio frequency (RF) technology, such as low on-resistance (resistive switching), high on-capacitance, a much broader operating temperature range than silicon electronic devices, high isolation (isolation is the amount of output signal when the switch is off [28]), and low insertion loss (insertion is characterized by the amount of losses in the signal output line when the switch is on [28]).

Areas of applications for capacitive microswitches are concentrated mainly on wireless communications and radar systems. Transmit/receive switches in a cellular phone are one example of such uses. In addition, these devices are excellent candidates to be used in phase shifting and time-delay circuits, such as in phased-array radars and communications antennas [29].

The structure of capacitive microswitches is close to that of resonant sensors, in which the actuated microbeam forms one side of an air-gap capacitor and the other side is a stationary electrode (substrate) connected to the output circuit. However, the actuation mechanism and the principle of operation are different from resonant sensors. Here, the actuation is achieved by applying a DC polarization voltage to the

microbeam to deflect it to contact the output circuit, at which the switch is in the on-state. When removing the DC voltage, the microbeam is released to its original position, at which the switch is in the off-state.

There are two ways in which capacitive microswitches can transmit electric signals [28]. First, the microbeam is completely pulled down by an electrostatic force until it contacts the output circuit and passes the signal, during which the switch is on. When the electrostatic force is removed, the elasticity of the microbeam pulls it back to its original equilibrium position, at which the switch is off. Typically, the microbeam is actuated by DC voltages higher than the pull-in voltage in order to snap it in a fast wide stroke. However, in some designs, the microswitch is actuated below the pull-in voltage to avoid problems that accompany pull-in switches, such as sticking and hysteresis. An example of such a design is found in [14].

The second way does not require a physical contact between the input and output circuits. It is based on changes in the capacitance of the airgap between the microbeam and the substrate of the output. When the microbeam is at rest, the capacitance of the airgap has a certain low value, during which the switch is off. When the microbeam is deflected downward, the capacitance has a much higher value, during which the switch is on.

The maximum working frequency and switching time are two important parameters in capacitive microswitches. The maximum working frequency is the highest frequency a microbeam can follow, beyond which the switch is either on or off. It relates to the fundamental natural frequency of the microbeam. The switching time is the time an unactuated microbeam takes to respond at a certain DC voltage and to transmit the electrical signal. Both parameters give important information about the range of application where the designed switches can be used. As an example, for the speed limitation, the switching time of capacitive microswitches is in the microsecond range, thus they cannot be used in high-speed applications. However, they are very sufficient for other applications, like beam steering in phase antennas.

We study the static behavior of microbeams in capacitive microswitches in Chapter 3. In Chapter 7, we use a reduced-order model to simulate the dynamic behavior of

microbeams and compute the time they need to reach pull-in.

Chapter 3

Problem Formulations

In this Chapter, we formulate the problems describing the behavior of microbeams in resonant sensors and capacitive microswitches. We also derive reduced-order models for simulating the mechanical behavior of microbeams under a DC electrostatic actuation.

First, we derive the equations that govern the static deflection of a microbeam under an electrostatic force. We also derive the equations describing its natural frequencies, mode shapes, and dynamic response. Then, we derive the equations that govern the dynamics of microbeams actuated by a combination of DC and AC electric forces. Finally, we discretize the equations of motion of electrostatically actuated microbeams by using the Galerkin procedure. We present two approaches to treat the electrostatic force term in the discretization. We show in Chapter 4 that only one of them predicts correct behaviors.

3.1 Resonant Sensors Model

We consider a resonant microbeam, Figure 3.1, actuated by an electric load composed of a DC component (polarization voltage) V_p and an AC component $v(t)$ and subject to viscous damping $\hat{c}$ per unit length.

We model the microbeam as a plate undergoing cylindrical bending under an applied load, which is constant along the width of the plate. Typical dimensions of resonators violate the basic assumptions of a beam model; the ratio of a typical mi-

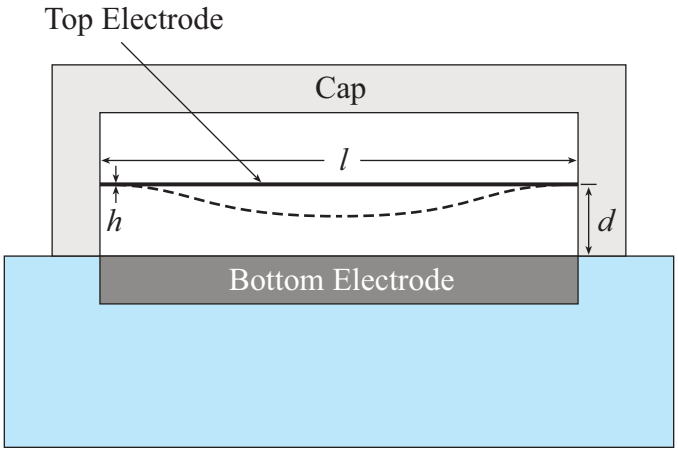

Figure 3.1: A schematic drawing of a resonant microbeam.

crobeam length ℓ to width b is < 10. The plate is clamped across its long ends and free across its width. We assume that the transverse deflection w of the plate is constant along the width, thus reducing the plate static deflection equation to [3]

$$\frac{EI}{1-\nu^2}\frac{\partial^4 w}{\partial x^4} = \left[\frac{EA}{2\ell(1-\nu^2)}\int_0^\ell \left(\frac{\partial w}{\partial x}\right)^2 dx + \hat{N}\right]\frac{\partial^2 w}{\partial x^2} \tag{3.1}$$

where x is the position along the plate length, A and I are the area and moment of inertia of the cross section, E is Young's modulus, ν is Poisson's ratio, and $\hat{N}$ is the applied axial force. The plate boundary conditions are

$$w(0,y) = w(\ell,y) = 0, \qquad \frac{\partial w(0,y)}{\partial x} = \frac{\partial w(\ell,y)}{\partial x} = 0 \tag{3.2}$$

Using the modified beam equation, we rewrite the equation of motion governing the transverse deflection of the microbeam under electric forces as

$$\begin{aligned}\frac{EI}{1-\nu^2}\frac{\partial^4 w}{\partial x^4} + \rho bh\frac{\partial^2 w}{\partial t^2} + \hat{c}\frac{\partial w}{\partial t} = &\left[\frac{EA}{2\ell(1-\nu^2)}\int_0^\ell \left(\frac{\partial w}{\partial x}\right)^2 dx + \hat{N}\right]\frac{\partial^2 w}{\partial x^2} \\ &+ \tfrac{1}{2}\epsilon_0\epsilon_r b\frac{(V_p + v(t))^2}{(d-w)^2}\end{aligned} \tag{3.3}$$

where $w(x,t)$ is the deflection of the microbeam, t is time, ρ is the material density,

h is the microbeam thickness, d is the gap width, ϵ_0 is the dielectric constant of vacuum, and ϵ_r is the relative dielectric constant of the gap medium to an air gap. The last term in equation (3.3) represents the parallel-plate electric forces neglecting the fringing effect of the electric field. We refer to Griffiths [30] for more information about the electric forces. The microbeam is assumed to be clamped at both ends; hence the boundary conditions are

$$w(0,t) = w(\ell,t) = 0, \qquad \frac{\partial w(0,t)}{\partial x} = \frac{\partial w(\ell,t)}{\partial x} = 0 \tag{3.4}$$

For convenience, we introduce the nondimensional variables (denoted by hats)

$$\hat{w} = \frac{w}{d}, \qquad \hat{x} = \frac{x}{\ell}, \qquad \hat{t} = \frac{t}{T} \tag{3.5}$$

where T is a time scale, which is defined below. Substituting equations (3.5) into equations (3.3) and (3.4) and dropping the hats, we obtain

$$\frac{\partial^4 w}{\partial x^4} + \frac{\partial^2 w}{\partial t^2} + c\frac{\partial w}{\partial t} = \left[\alpha_1 \Gamma(w,w) + N\right]\frac{\partial^2 w}{\partial x^2} + \alpha_2 \frac{(V_p + v(t))^2}{(1-w)^2} \tag{3.6a}$$

$$w(0,t) = w(1,t) = 0, \qquad \frac{\partial w(0,t)}{\partial x} = \frac{\partial w(1,t)}{\partial x} = 0 \tag{3.6b}$$

where

$$\Gamma\left(f_1(x,t), f_2(x,t)\right) = \int_0^1 \frac{\partial f_1}{\partial x}\frac{\partial f_2}{\partial x} dx \tag{3.6c}$$

Equation (3.6a) is a nondimensional integral-partial-differential equation with linear and nonlinear terms as well as external and parametric excitation terms. The nondimensional parameters appearing in equation (3.6a) are

$$c = \frac{\hat{c}\ell^4(1-\nu^2)}{EIT},\ \alpha_1 = 6\left(\frac{d}{h}\right)^2,\ N = \frac{\hat{N}\ell^2(1-\nu^2)}{EI},$$
$$\alpha_2 = \frac{6\epsilon_0\epsilon_r\ell^4(1-\nu^2)}{Eh^3d^3} \tag{3.7}$$

and T is chosen as $T = \left(\frac{\rho b h \ell^4(1-\nu^2)}{EI}\right)^{\frac{1}{2}}$

The microbeam deflection under an electric force is composed of a static component due to the DC voltage, denoted by $w_s(x)$, and a dynamic component due to the AC voltage, denoted by $u(x,t)$; that is,

$$w(x,t) = w_s(x) + u(x,t) \tag{3.8}$$

To calculate the static deflection of the microbeam, we set the time derivatives and the AC forcing term in equation (3.6a) equal to zero and obtain

$$\frac{d^4 w_s}{dx^4} = \left[\alpha_1 \Gamma(w_s, w_s) + N\right] \frac{d^2 w_s}{dx^2} + \frac{\alpha_2 V_p^2}{\left(1 - w_s\right)^2} \tag{3.9a}$$

It follows from equations (3.6b) and (3.8) that the boundary conditions are

$$w_s = 0 \text{ and } \frac{dw_s}{dx} = 0 \text{ at } x = 0 \text{ and } x = 1 \tag{3.9b}$$

We generate the problem governing the dynamic behavior of the microbeam around the deflected shape by substituting equation (3.8) into equations (3.6) and using equation (3.9a) to eliminate the terms representing the equilibrium position. To third-order in u, the result is

$$\begin{aligned} \frac{\partial^2 u}{\partial t^2} + c\frac{\partial u}{\partial t} + \frac{\partial^4 u}{\partial x^4} &= \left(\alpha_1 \Gamma\left(w_s, w_s\right) + N\right) \frac{\partial^2 u}{\partial x^2} + 2\alpha_1 \Gamma\left(w_s, u\right) \frac{d^2 w_s}{dx^2} \\ &+ \frac{2\alpha_2 V_p^2}{\left(1 - w_s\right)^3} u + \alpha_1 \Gamma\left(u, u\right) \frac{d^2 w_s}{dx^2} + 2\alpha_1 \Gamma\left(w_s, u\right) \frac{\partial^2 u}{\partial x^2} \\ &+ \frac{3\alpha_2 V_p^2}{\left(1 - w_s\right)^4} u^2 + \alpha_1 \Gamma\left(u, u\right) \frac{\partial^2 u}{\partial x^2} + \frac{4\alpha_2 V_p^2}{\left(1 - w_s\right)^5} u^3 \\ &+ \frac{2\alpha_2 V_p}{\left(1 - w_s\right)^2} v(t) + \frac{4\alpha_2 V_p}{\left(1 - w_s\right)^3} v(t) u + \cdots \end{aligned} \tag{3.10a}$$

$$u(0,t) = u(1,t) = 0, \qquad \frac{\partial u(0,t)}{\partial x} = \frac{\partial u(1,t)}{\partial x} = 0 \tag{3.10b}$$

Equations (3.9) and (3.10) indicate that various design parameters influence the system in different ways. The axial force enters the equations governing the static

deflection and dynamic motion of the microbeam linearly. On the other hand, the length of the microbeam has a significant impact on both the static and dynamic components of the electric force, as can be seen from the definition of α_2 in equation (3.7). The influence of the mid-plane stretching is dependent on the *ratio* α_1 of the air gap distance d to the microbeam thickness h rather than on their actual values. Increasing this ratio amplifies the influence of the mid-plane stretching and vice versa. On the other hand, the electric force depends on the product of h and d; that is, their actual values.

To obtain the microbeam linear mode shapes and the corresponding natural frequencies, we drop the nonlinear, forcing, and damping terms in equation (3.10a) and obtain the linear-undamped eigenvalue problem

$$\frac{\partial^4 u}{\partial x^4} - (\alpha_1\Gamma_1 + N)\frac{\partial^2 u}{\partial x^2} - \frac{2\alpha_2 V_p^2}{(1-w_s)^3}u - 2\alpha_1\Gamma\left(w_s, u\right)\frac{d^2 w_s}{dx^2} = -\frac{\partial^2 u}{\partial t^2} \tag{3.11a}$$

$$u = 0 \text{ and } \frac{\partial u}{\partial x} = 0 \text{ at } x = 0 \text{ and } x = 1 \tag{3.11b}$$

where $\Gamma_1 = \Gamma\left(w_s, w_s\right)$. We solve equations (3.11) for the undamped mode shapes and natural frequencies under the static deflection distribution $w_s(x)$. Assuming a harmonic motion in the nth mode in the form

$$u(x,t) = \phi_n(x)e^{i\omega_n t} \tag{3.12}$$

where $\phi_n(x)$ is the nth mode shape and ω_n is the nth nondimensional natural frequency, we reduce equations (3.11) to

$$\phi_n^{iv} - (\alpha_1\Gamma_1 + N)\phi_n'' - \frac{2\alpha_2 V_p^2}{(1-w_s)^3}\phi_n - 2\alpha_1\Gamma_2 w_s'' = \omega_n^2\phi_n \tag{3.13a}$$

$$\phi_n = 0 \text{ and } \phi_n' = 0 \qquad \text{at} \qquad x = 0 \text{ and } x = 1 \tag{3.13b}$$

where $\Gamma_2 = \Gamma\left(w_s, \phi_n\right)$ and the prime denotes the derivative with respect to x.

3.2 Capacitive Microswitch Models

3.2.1 Continuous System Model

Here we consider a fixed-fixed microbeam actuated by a DC electrostatic force. To derive the problem governing the microbeam motion, we set the AC force component $u(t)$ in equations (3.6) equal to zero and obtain

$$\frac{\partial^4 w}{\partial x^4} + \frac{\partial^2 w}{\partial t^2} + c\frac{\partial w}{\partial t} = \left[\alpha_1 \Gamma(w,w) + N\right] \frac{\partial^2 w}{\partial x^2} + \alpha_2 \frac{V_p^2}{(1-w)^2} \tag{3.14a}$$

$$w(0,t) = w(1,t) = 0, \qquad \frac{\partial w(0,t)}{\partial x} = \frac{\partial w(1,t)}{\partial x} = 0 \tag{3.14b}$$

Equation (3.14a) is an integral-partial-differential equation that describes the microbeam dynamic behavior.

We note that by setting the time derivatives equal to zero in equations (3.14), we obtain the same static equation for resonant microbeams; that is, equations (3.9). Similarly, the problem that describes the mode shapes and natural frequencies of the microbeam as a function of the static deflection is given by equations (3.13).

3.2.2 Reduced-Order Models (Macromodels)

In this Section, we discretize equations (3.14). Our motivation for the discretization stems from the need to study the transient behavior of the microbeam in response to the DC forcing. Toward this, we reduce the continuous system, which is governed by an integral-partial differential equation and associated boundary conditions, into a finite-degree-of-freedom system consisting of ordinary-differential equations in time. Then, we integrate this system to simulate the transient behavior. This is the idea behind using reduced-order models, also called macromodels, for studying the behavior of continuous systems. This technique and its application to nonlinear systems is discussed by Nayfeh and Mook [31].

We use the undamped linear mode shapes of the undeflected microbeam as basis functions in the Galerkin procedure. However, the mode shapes of a microbeam are functions of the deflection and might differ significantly from the undeflected mode

shapes near pull-in. Hence, a question arises on how accurate are the predicted motions obtained using the mode shapes of the undeflected microbeam close to pull-in. To answer this question, we need to compare the obtained results with experimental results or results based on simulating the distributed-parameter system. Fortunately, as is shown in Chapter 4, the undeflected linear mode shapes turn out to be sufficient to represent the motion.

We propose two methods to treat the term $\frac{1}{(1-w)^2}$ in the electrostatic force in the discretization procedure. Beginning with the first method, we expand $\frac{1}{(1-w)^2}$ in a Taylor series around $w = 0$. The problem associated with this method is that w becomes close to 1 near pull-in. Thus, this expansion is expected to breakdown for large deflections near pull-in.

Here, we expand the electrostatic force in equation (3.14a) up to fifth order and obtain

$$\frac{\partial^4 w}{\partial x^4} + \frac{\partial^2 w}{\partial t^2} + c\frac{\partial w}{\partial t} = [\alpha_1 \Gamma(w,w) + N]\frac{\partial^2 w}{\partial x^2} + \alpha_2 V_p^2 \left(1 + 2w + 3w^2 + 4w^3 + 5w^4 + 6w^5\right) \tag{3.15}$$

Then, we express the solution of equations (3.15) and (3.14b) as

$$w(x,t) = \sum_{i=1}^{N} u_i(t)\phi_i(x) \tag{3.16}$$

where $\phi_i(x)$ is the ith linear undamped mode shape of the undeflected microbeam and is normalized such that $\int_0^1 \phi_i^2 dx = 1$. Setting V_p and w_s in equations (3.13) equal to zero, we obtain the following linear undamped eigenvalue problem of a straight beam:

$$\phi_i^{iv} = N\phi'' + \omega_i^2 \phi_i \tag{3.17a}$$

$$\phi_i = 0 \text{ and } \phi_i' = 0 \qquad \text{at} \qquad x = 0 \text{ and } x = 1 \tag{3.17b}$$

Substituting equation (3.16) into equation (3.15), using equation (3.17a), multiplying

the result by $\phi_n(x)$, and integrating the outcome from x= 0 to 1, we obtain

$$\ddot{u}_n + \omega_n^2 u_n + c\dot{u}_n = \alpha_2 V_p^2 \int_0^1 \phi_n dx + 2\alpha_2 V_p^2 u_i + 3\alpha_2 V_p^2 u_i u_j \int_0^1 \phi_n \phi_i \phi_j dx$$
$$+ u_i u_j u_k \left[\alpha_1 \Gamma(\phi_i, \phi_j) \int_0^1 \phi_n \phi_k^{''} dx + 4\alpha_2 V_p^2 \int_0^1 \phi_n \phi_i \phi_j \phi_k dx \right]$$
$$+ 5\alpha_2 V_p^2 u_i u_j u_k u_l \int_0^1 \phi_n \phi_i \phi_j \phi_k \phi_l dx$$
$$+ 6\alpha_2 V_p^2 u_i u_j u_k u_l u_m \int_0^1 \phi_n \phi_i \phi_j \phi_k \phi_l \phi_m dx \qquad n = 1, 2, \ldots \quad (3.18)$$

where Γ is defined in equation (3.6c). Equations (3.18) represent a discretized system of ordinary-differential equations, which contains all nonlinearities up to fifth order.

In the second method of treating the electrostatic force term, we multiply equation (3.14a) by $(1-w)^2$ so that the electrostatic force is represented exactly. The disadvantage of this method is that, when discretizing the system, the mass matrix of the resulting equations is no longer diagonal, and hence the numerical integration of the resulting system is more complicated.

Multiplying equation (3.14a) by $(1-w)^2$, substituting equations (3.16) and (3.17a) into the resulting equation, multiplying by $\phi_n(x)$, and integrating the outcome from x= 0 to 1, we obtain

$$\ddot{u}_n - 2\ddot{u}_i u_j \int_0^1 \phi_i \phi_j \phi_n dx + \ddot{u}_i u_j u_k \int_0^1 \phi_i \phi_j \phi_k \phi_n dx = \alpha_2 V_p^2 \int_0^1 \phi_n dx - u_n \omega_n^2 - c\dot{u}_n$$
$$+ 2u_i u_j \omega_i^2 \int_0^1 \phi_i \phi_j \phi_n dx - u_i u_j u_k \omega_i^2 \int_0^1 \phi_i \phi_j \phi_k \phi_n dx + 2c\dot{u}_i u_j \int_0^1 \phi_i \phi_j \phi_n dx$$
$$- c\dot{u}_i u_j u_k \int_0^1 \phi_i \phi_j \phi_k \phi_n dx + \alpha_1 u_i u_j u_k \Gamma(\phi_i, \phi_j) \int_0^1 \phi_n \phi_k^{''} dx$$
$$- 2\alpha_1 u_i u_j u_k u_l \Gamma(\phi_i, \phi_j) \int_0^1 \phi_k \phi_l^{''} \phi_n dx + \alpha_1 u_i u_j u_k u_l u_m \Gamma(\phi_i, \phi_j) \int_0^1 \phi_k^{''} \phi_l \phi_m \phi_n dx$$
$$n = 1, 2, \ldots \quad (3.19)$$

We note that the coupling of the system of equations (3.19) is stronger than that of equations (3.18), because of the nonlinear inertia terms. Moreover, the nonlinear terms in equations (3.18) depend on where the electrostatic force expansion is truncated.

However, in the second method, the nonlinearity always has the same form, which includes nonlinearities up to fifth order.

Chapter 4

Static Response of Microbeams to a DC Electrostatic Force

In this Chapter, we study the static behavior of a microbeam in response to a DC electrostatic force. First, we present a numerical procedure to solve directly the boundary-value problem governing the static deflection. We validate our method by comparing our theoretical results with experimental results available in the literature. We use the numerical scheme to investigate the effect of the nondimensional design parameters on the static deflection and pull-in. Then, we discuss new methods to treat the same problem using a reduced-order model based on the discretized systems derived in Chapter 3. Finally, we compare all presented methods.

4.1 A Shooting Method for Solving the Static Boundary-Value Problem

4.1.1 Numerical Scheme

Equations (3.9) describe the microbeam deflection under static loading. We use a shooting method to solve the problem numerically for $w_s(x)$. We assume an initial deflection distribution $w_s^0(x)$ and use it to evaluate $\Gamma^1 = \Gamma\left(w_s^0, w_s^0\right)$. In each iteration, we substitute the iterated value of the integral Γ^i into equation (3.9a), solve the

nonlinear boundary-value problem

$$\frac{d^4 w_s}{dx^4} = \left(\alpha_1 \Gamma^i + N\right) \frac{d^2 w_s}{dx^2} + \frac{\alpha_2 V_p^2}{\left(1 - w_s\right)^2} \tag{4.1a}$$

$$w_s = w_s' = 0 \qquad \text{at} \qquad x = 0 \text{ and } x = 1 \tag{4.1b}$$

numerically for $w_s^i(x)$, and then calculate a new $\Gamma^{i+1} = \Gamma\left(w_s^i, w_s^i\right)$. We continue to iterate (shoot) on the integral $\Gamma\left(w_s, w_s\right)$ until it converges to a value within predefined tolerance.

There are two problems associated with the proposed numerical method. The first is the sensitivity of the solution to the initial guess as pull-in is approached. We note that the domain of attraction of the solution narrows as $\alpha_2 V_p^2$ increases and becomes very narrow close to pull-in. Hence, it becomes very difficult to find a suitable initial guess that makes the numerical scheme converges. The second is related to the stiffness of the problem. As the values of α_1 and $\alpha_2 V_p^2$ increase, the boundary-value problem becomes stiffer. Accordingly, at high α_1, choosing initial condition that lead to convergence become difficult.

The numerical solution of equations (4.1) reveals the exitance of two solutions (upper branch and lower branch) for each value of V_p. Both solutions seem to coalesce at the pull-in voltage. However, as aforementioned, it becomes difficult using our numerical method to calculate the static deflection very close to pull-in, and hence to determine the exact location of the pull-in voltage.

The stability of the upper-branch solution, which cannot be observed experimentally, is studied in the next Chapter where we show that it is unstable. Hence, in what follows, we disregard the upper-branch solution and refer to the lower-branch solution as the microbeam static deflection. Next, we study the effect of the nondimensional design parameters on the static deflection and pull-in.

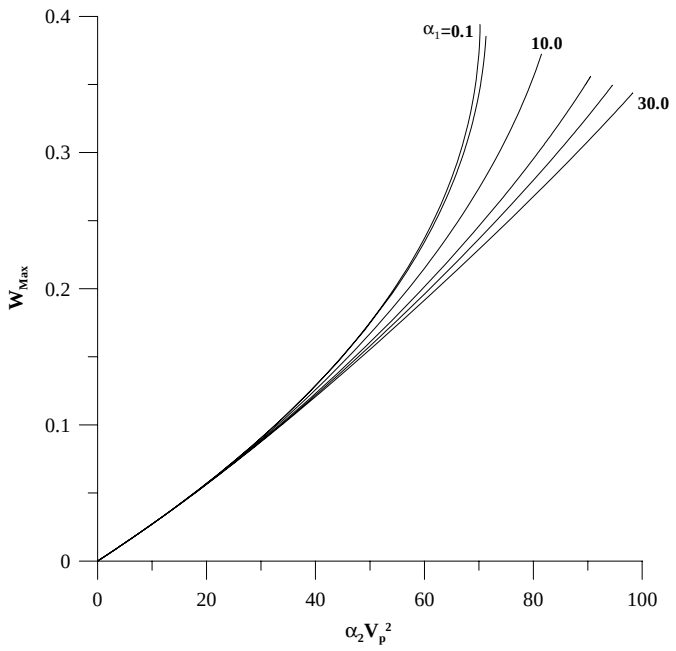

Figure 4.1: Variation of the maximum nondimensional deflection W_{Max} with $\alpha_2 V_p^2$ for α_1 of 0.1, 1.0, 10.0, 20.0, 25.0, and 30.0 and no axial load.

4.1.2 Effect of the Nondimensional Design Parameters on the Static Behavior

To study the influence of the mid-plane stretching on the static deflection, we solved equations (4.1) for a range of electrostatic forces varying from zero to the forcing level where structural instability (pull-in) develops. No axial loads were applied to the microbeam. This procedure was repeated for various values of α_1, the ratio of the air-gap distance to the microbeam thickness. Figure 4.1 shows variation of the maximum nondimensional deflection $W_{Max} = w_s\left(x = \frac{\ell}{2}\right)$ with $\alpha_2 V_p^2$ for various values of α_1. As the electrostatic force, represented by $\alpha_2 V_p^2$, increases, the maximum deflection increases. This relationship is linear at low levels of electrostatic forcing; however as the electrostatic force increases, the relationship becomes increasingly nonlinear. As a result, the slope $\frac{\partial W_{Max}}{\partial\left(\alpha_2 V_p^2\right)}$ of the curve grows from a small positive value and approaches infinity at pull-in. This is seen more clearly for small values of α_1, where the problem is less stiffer, and hence we were able to obtain solutions very close to pull-in. Figure

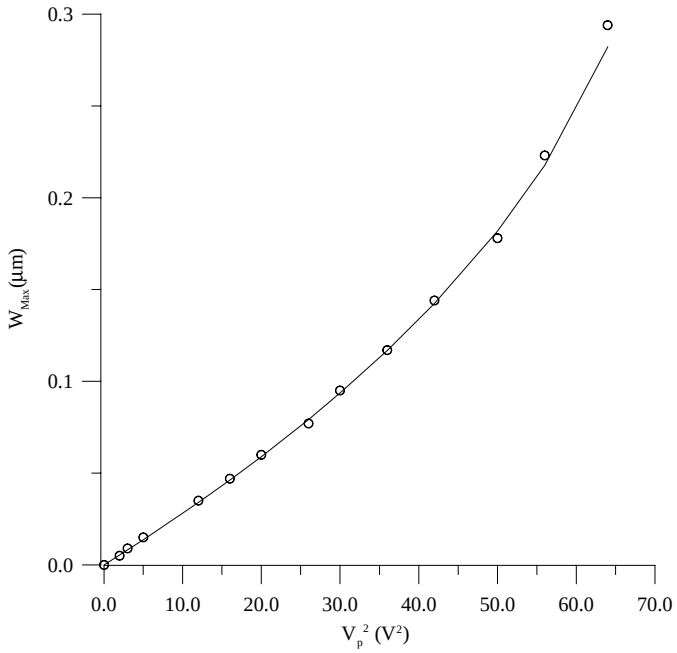

Figure 4.2: Comparison of the maximum deflection W_{Max} calculated using our model (solid line) with that calculated by Choi and Lovell [5] (circles) for $\alpha_1 = 1.5$ and $N = 0$.

4.1 also shows that increasing α_1 narrows the nonlinear region of W_{Max}.

Figure 4.2 compares the maximum deflection calculated using our approach with the analytical results reported by Choi and Lovell [8] for the same values of α_1 and V_p^2 and no axial load. There is excellent agreement between the two sets of results.

To study the influence of axial loading on the microbeam behavior, we hold α_1 constant and solve equations (4.1) for various values of N, the nondimensional axial force, over a range of electrostatic forces varying from zero to the forcing level where structural instability (pull-in) develops. Figure 4.3 shows variation of the maximum nondimensional deflection with $\alpha_2 V_p^2$ for various values of N. As the axial force increases from a negative value (compressive load) to a positive value (tensile load), both the slope of the linear region and the curvature of the nonlinear region decrease. Further, the level of the electrostatic force at pull-in increases as the axial force increases.

Using a linear spring-mass model for an electrostatically actuated microbeam, Seeger and Crary [32] reported that the pull-in instability develops beyond a static

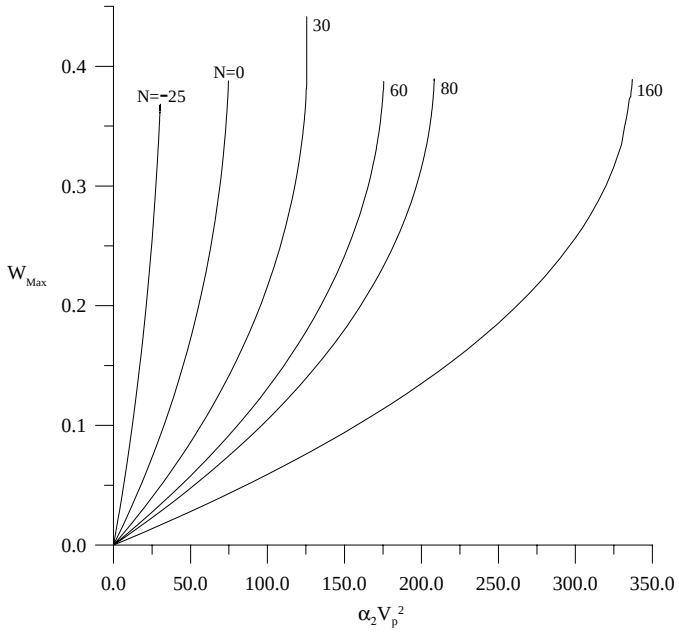

Figure 4.3: Variation of the maximum nondimensional deflection W_{Max} with $\alpha_2 V_p^2$ when $\alpha_1 = 3.7$ for various axial forces.

deflection limit of $W_{Max} \leq \frac{1}{3}$. However, our results in Figures 4.1 and 4.3 show maximum deflection values beyond that limit and up to 0.4. These results indicate that failure to account for geometric nonlinearities, the actual deflection distribution, and the mid-plane stretching leads to an underestimation of the stability limits of the microbeam.

Figure 4.4 shows variation of $\alpha_2 V_p^2$, representing the electrostatic force at pull-in, with the axial load for various values of α_1. Increasing α_1 and/or N increases the level of the electrostatic forcing at pull-in. Further, it demonstrates a linear relationship between the axial load and the pull-in level.

Sometimes in the literature, for example [20], an applied axial force is added to a microbeam model to compensate for the neglected mid-plane stretching by matching the theoretical and experimental pull-in voltages. As seen in Figures 4.1-4.4, although the pull-in voltage can be increased by either increasing α_1 or by N, they are not equivalent and each has a totally different behavior. Thus, compensating for mid-plane stretching by an axial force might produce errors.

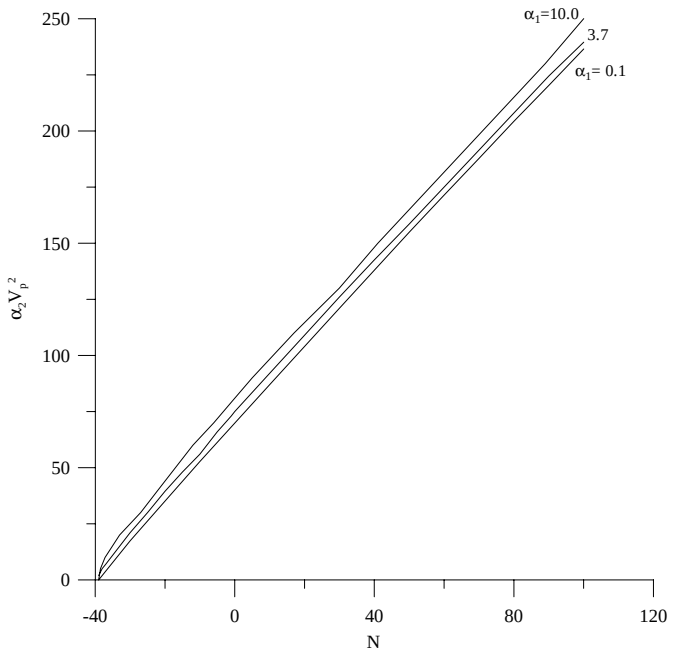

Figure 4.4: Variation of the level of electrostatic forcing, represented by $\alpha_2 V_p^2$, at pull-in with the axial force for $\alpha_1 = 0.1, 3.7$ and 10.0.

4.2 Reduced-Order Models for Simulating the Microbeams Static Behavior

We derived in Chapter 3 two discretized systems of equations describing the motion of microbeams under a DC electrostatic force. In this Section, we utilize these equations to obtain algebraic systems of equations, which are solved to simulate the microbeam static behavior. We discuss the two methods of discretization and show that only one of them can be used to predict the correct behavior.

We begin with the first method, which is based on expanding $\frac{1}{(1-w)^2}$ in a Taylor-series around w=0, and consider equations (3.18). Because the shape of microbeams during the motion is symmetric, we choose to use symmetric modes only.

To derive the discretized static equations, we make the $u_i(t)$ independent of time,

set all time derivatives equal to zero in equation (3.18), and obtain

$$\begin{aligned}\omega_n^2 u_n = {} & \alpha_2 V_p^2 \int_0^1 \phi_n dx + 2\alpha_2 V_p^2 u_i + 3\alpha_2 V_p^2 u_i u_j \int_0^1 \phi_n \phi_i \phi_j dx \\ & + u_i u_j u_k \left[\alpha_1 \Gamma(\phi_i, \phi_j) \int_0^1 \phi_n \phi_k'' dx + 4\alpha_2 V_p^2 \int_0^1 \phi_n \phi_i \phi_j \phi_k dx \right] \\ & + 5\alpha_2 V_p^2 u_i u_j u_k u_l \int_0^1 \phi_n \phi_i \phi_j \phi_k \phi_l dx \\ & + 6\alpha_2 V_p^2 u_i u_j u_k u_l u_m \int_0^1 \phi_n \phi_i \phi_j \phi_k \phi_l \phi_m dx \qquad n = 1, 2, \ldots \end{aligned} \tag{4.2}$$

Equations (4.2) represent a set of nonlinear algebraic equations. First, we solve the linear-undamped eigenvalue problem, equations (3.17), for the symmetric mode shapes ϕ_i and the corresponding natural frequencies ω_i. Then, we plug the results into equations (4.2) and solve them numerically for the unknowns u_i. Finally, from equation (3.16), we obtain the microbeam static deflection for any DC voltage V_p.

To determine the number of terms in the Taylor-series expansion, we computed the microbeam deflection near the pull-in voltage using four, five, and six terms and compared the results with those obtained by solving the boundary-value problem using a shooting method. However, very close to pull-in, where the nondimensional deflection approaches unity, we could not find a good initial guess of the static deflection, and hence we were unable to obtain results using the shooting method. Therfore, we could not compare results very close to pull-in. The maximum deflection obtained using four and five terms are less than that obtained using the shooting method, indicating that the electrostatic force is incompletely represented. On the other hand, the results of the six-term expansion are almost the same as those obtained with the shooting method. Thus, we adopt to expand $\frac{1}{(1-w)^2}$ up to six terms.

In Figure 4.5, we compare the calculated maximum nondimensional deflection W_{Max} of a microbeam for various values of V_p using the first 3 symmetric modes with results obtained by using the shooting method. We used a microbeam with the parameters $L = 610\mu m$, $h = 2.1\mu m$, $b = 40\mu m$, and $d = 2.3\mu m$. The microbeam is subject to an axial stress of -3.7 MPa. We note from Figure 4.5 that the results obtained using this discretized method are in poor agreement with those obtained by solving

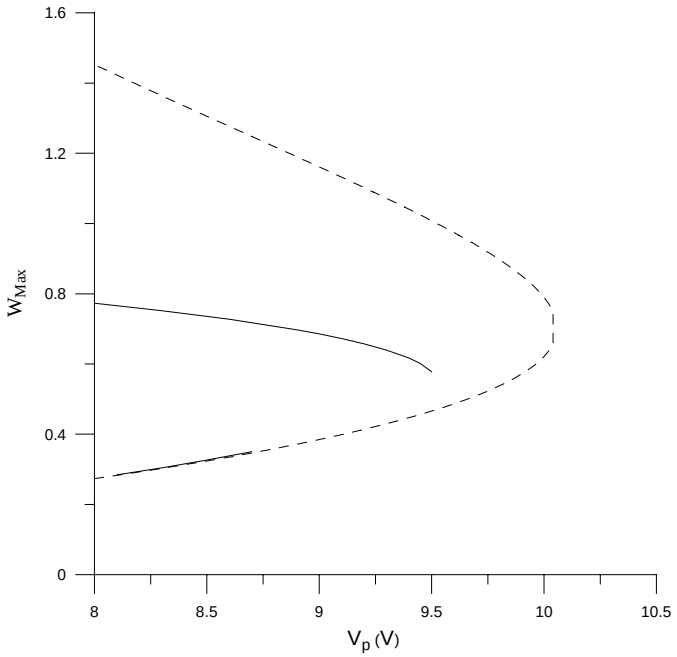

Figure 4.5: Comparison of the calculated maximum nondimensional deflection W_{Max} (dashed line) using a three-symmetric-mode discretized system of equations, equations 4.2, with that obtained by solving the static boundary-value problem using a shooting method (solid lines) for various values of V_p. The electrostatic force term $\frac{1}{(1-w)^2}$ was expanded using a Taylor series around w=0 up to fifth order .

the boundary-value problem. The predicted lower branches are very close away from pull-in, but they seem to deviate increasingly as pull-in is approached. However, the predicted upper branches are far away from each other. This is because w approaches 1 there, and thus the Taylor-series expansion breaks down and the approximation of the electrostatic force becomes incorrect.

We conclude that expanding $\frac{1}{(1-w)^2}$ in a Taylor series around w=0 is an improper way to represent the electrostatic force. Discretizing the equation of motion using this method with the undamped linear mode shapes of an undeflected microbeam may lead to incorrect results.

We move now to discuss the second discretization method, which is based on multiplying equations (3.19) by $(1-w)^2$, and hence representing the electrostatic force in the discretized equations without approximation. Considering equations (3.19), we let

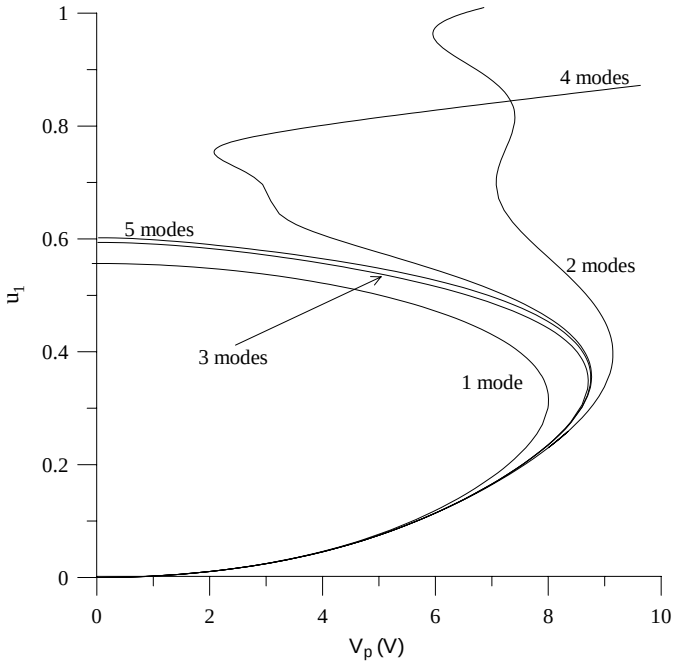

Figure 4.6: The influence of the number of symmetric modes retained in the discretization on the variation of u_1 with V_p.

the u_i be independent of time, set all time derivatives equal to zero, and obtain

$$u_n\omega_n^2 = \alpha_2 V_p^2 \int_0^1 \phi_n dx + 2u_i u_j \omega_i^2 \int_0^1 \phi_i\phi_j\phi_n dx - u_i u_j u_k \omega_i^2 \int_0^1 \phi_i\phi_j\phi_k\phi_n dx$$
$$+ \alpha_1 u_i u_j u_k \Gamma(\phi_i,\phi_j) \int_0^1 \phi_n \phi_k'' dx - 2\alpha_1 u_i u_j u_k u_l \Gamma(\phi_i,\phi_j) \int_0^1 \phi_k \phi_l'' \phi_n dx$$
$$+ \alpha_1 u_i u_j u_k u_l u_m \Gamma(\phi_i,\phi_j) \int_0^1 \phi_k'' \phi_l \phi_m \phi_n dx \qquad n = 1, 2, \ldots \tag{4.3}$$

Equations (4.3) are nonlinear algebraic equations. We follow the same procedure used in the first method for calculating the static deflection w. We also use symmetric modes in the discretization.

Figure 4.6 shows a plot of u_1, which is the dominant coefficient, obtained by solving equations (4.3) for various values of V_p using one-, two-, three-, four-, and five-mode discretization. We used the same design specifications used in Figure 4.5. As can be seen, using an even number of modes predicts an erroneous upper branch and

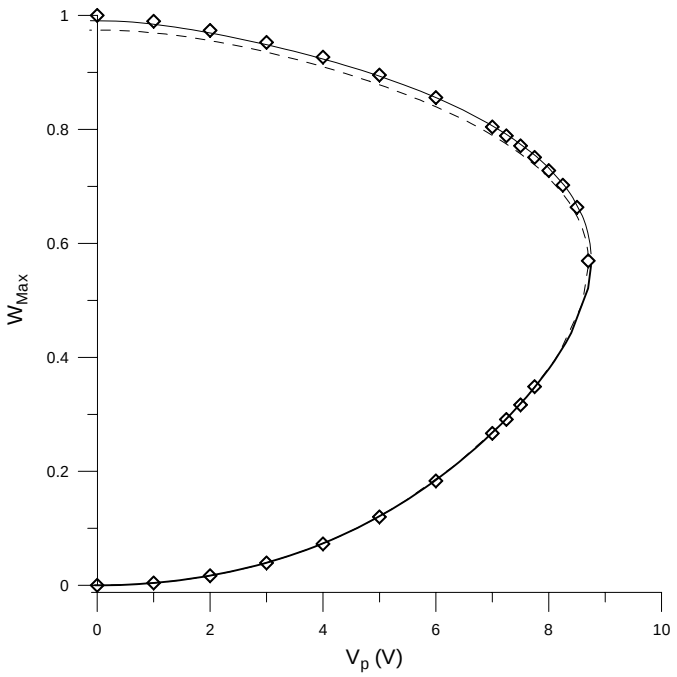

Figure 4.7: Variation of W_{Max} calculated with the second discretization method using linear symmetric modes for two cases: the first uses the first three modes (dashed line) and the second uses the first five modes (solid line). The two curves are compared with results obtained by solving the boundary-value problem using a shooting method (diamonds).

an inaccurate lower branch, despite the fact that all of the used mode shapes are symmetric. Unfortunately, there is no clear reason for this strange behavior. Figure 4.6 also shows the predicted branches converge with increasing number of modes as long as this number is odd.

In Figure 4.7, we compare W_{Max} calculated with the second discretization method using the first three modes (dashed line) and the first five modes (solid line) with results obtained by solving the boundary-value problem using a shooting method (diamonds). It is clear that the five-mode solution is in excellent agreement with the results of the shooting method.

We conclude that discretizing the equation of motion after multiplying it by $(1-w)^2$ predicts successfully the static behavior of microbeams by using no more than five modes. This is very significant result. It demonstrates a way of using the linear

undamped mode shapes of undeflected microbeams to generate reduced-order models for predicting the behavior of electrostatic MEMS. Mehner et al. [24] mentioned that the linear normal modes do not provide an adequate basis set to compute the elastic stored energy in stress-stiffened cases. They [23] indicated that using the linear normal modes does not yield correct results beyond 30% of the pull-in voltage. However, our results show that the linear normal modes yield correct results up to the pull-in voltage, provided that the model accounts for the mid-plane stretching and that the electrostatic force is properly treated in the discretization procedure. The use of the linear mode shapes of an undeflected microbeam as basis functions is much more convenient than running finite-element codes to extract such functions [24].

Solving an algebraic system of equations to simulate the static behavior has the advantage of being stable and unaffected by the pull-in instability, unlike the shooting method presented here or other finite-element based softwares used in the literature. As shown in Figures 4.1-4.3, we were not able to obtain results using the shooting method beyond W_{Max}=0.4. This is because it becomes very difficult to find a suitable initial guess that converges to a solution besides the fact that the problem becomes very stiff. However using the second discretization method, we can simulate the behavior very close to pull-in, thereby enabling a precise prediction of the pull-in voltage, corresponding to the coalescence of the two branches. To verify the results obtained by the second discretization method near pull-in, we calculated Γ_1 using the value of w_s obtained with the second method and used both as initial guesses to solve equations (4.1) by the shooting method. We found that the numerical scheme converges there.

As aforementioned, solutions of the boundary-value problem using our shooting method are very sensitive at high values of α_1 and close to pull-in because the problem becomes very stiff and it is difficult to find a suitable initial guess. The second discretization method however does not have such a problem. Figure 4.8 shows a plot of W_{Max} calculated using the second discretization method for α_1=50, α_2=3.904, and no axial load. The pull-in voltage is approximately at V_p =6.67 V. Using the shooting method, however, we are unable to obtain results beyond V_p= 5.3 V. Hence, assuming the pull-in voltage to be the value of voltage beyond which the numerical solver does

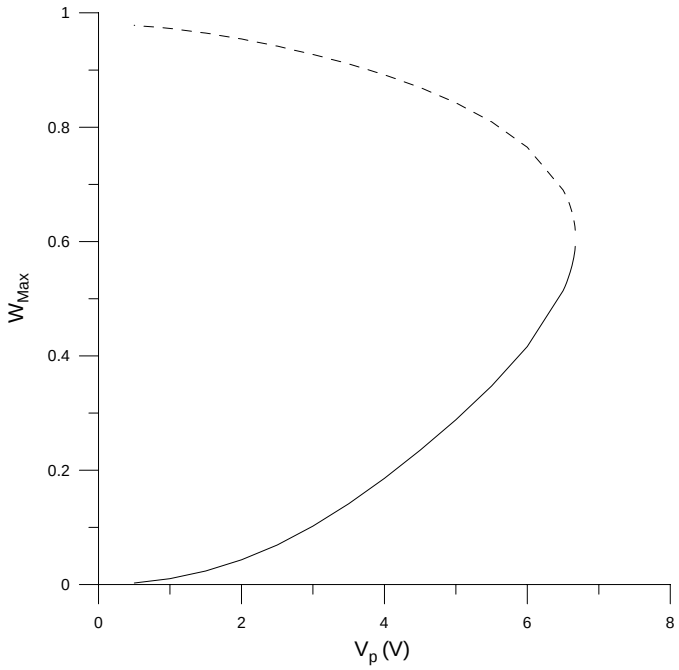

Figure 4.8: Variations of W_{Max} calculated using the second discretization method for various values of V_p and α_1=50, α_2=3.904, and no axial load. The dashed line denotes an unstable solution and the solid line denotes a stable solution.

not converge, which is the basis of most available finite-element-based packages in the literature, may give erroneous results.

Another advantage to using a discretized system of equations is the ability to study the stability of the obtained deflections and, in general, investigate possible nonlinear phenomena. As an example, we studied the local stability of the two solutions obtained by solving the algebraic system of equations (4.3). We calculated the Jacobian matrix of the discretized system of equations associated with each solution and computed its eigenvalues. The results show that one eigenvalue corresponding to the upper branch is always positive, and hence the solution is unstable. All of the eigenvalues of the lower branch are always real and negative, and hence it corresponds to stable nodes. At pull-in, both solution branches coalesce and one eigenvalue tends to zero. Thus, the pull-in voltage corresponds to a saddle-node bifurcation. Figure 4.8 shows a typical bifurcation diagram for such a saddle-node bifurcation, where the control parameter is $\alpha_2 V_p^2$. The dashed line denotes an unstable solution and the solid line denotes a stable

solution.

One more attractive feature that characterizes the presented reduced-order model is the fact that it is computationally very fast. The total time it takes to run our program codes in MATHMATICA to simulate the static behavior of a microbeam does not exceed few minutes, significantly shorter than the time other programs require to perform the same task.

Chapter 5

Natural Frequencies and Mode Shapes of Microbeams under a DC Electrostatic Force

In this chapter, we determine the natural frequencies and mode shapes of microbeams under a DC electrostatic force. We study the effect of the nondimensional design parameters on the natural frequencies and mode shapes. Also, we compare our theoretical results with available experimental results. Then, we discuss a mathematical relation between the static boundary-value problem and the eigenvalue problem.

5.1 Numerical Results

We first solved equations (3.9) for the static deflection w_s. Then, we solved equations (3.13) for each mode shape ϕ_n and the associated natural frequency ω_n using a combination of a shooting method and iteration on Γ_2 until Γ_2 converges to within predefined tolerances.

In Figure 5.1, we compare the normalized fundamental natural frequency $\frac{\omega_1}{\omega}$, where ω is the fundamental natural frequency at zero DC voltage, calculated using our model (solid lines) with the theoretical (dashed lines) and experimental results of Tilmans and Legtenberg [7] for a $210\mu m$ length microbeam (circles) and a $510\mu m$ length microbeam

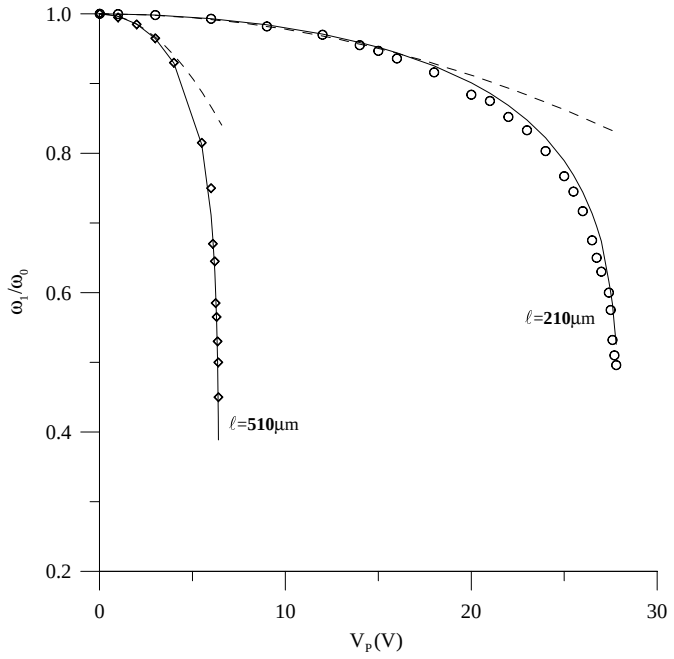

Figure 5.1: Comparison of the normalized fundamental natural frequency calculated using our model (solid lines) with those obtained theoretically (dashed lines) and experimentally by Tilmans and Legtenberg [7] for a $210\mu m$ length microbeam (circles) and for a $510\mu m$ length microbeam (diamonds).

(diamonds). For both microbeams, $h = 1.5\mu m, b = 100\mu m, d = 1.18\mu m$, and $\hat{N} = 0.0009N$. There is good agreement between our results and the experimental results, even as the microbeams approach their stability limits.

Figure 5.2 shows variation of the fundamental natural frequency of the microbeam with $\alpha_2 V_p^2$ for various values of α_1. For low α_1, the fundamental natural frequency of the microbeam tends to decrease as the electrostatic force increases and approaches zero as pull-in develops. As α_1 increases, the fundamental natural frequency increases for the same level of electrostatic forcing. At high values of α_1, $\alpha_1 \geq 22.0$, the fundamental natural frequency increases as the electrostatic force increases. This is due to the fact that, in this range, the effect of the mid-plane stretching dominates that of the electrostatic forcing. However, for large values of $\alpha_2 V_p^2$, the electrostatic force is expected to eventually dominate mid-plane stretching, and the fundamental natural frequency is expected to decrease and approach zero as pull-in develops.

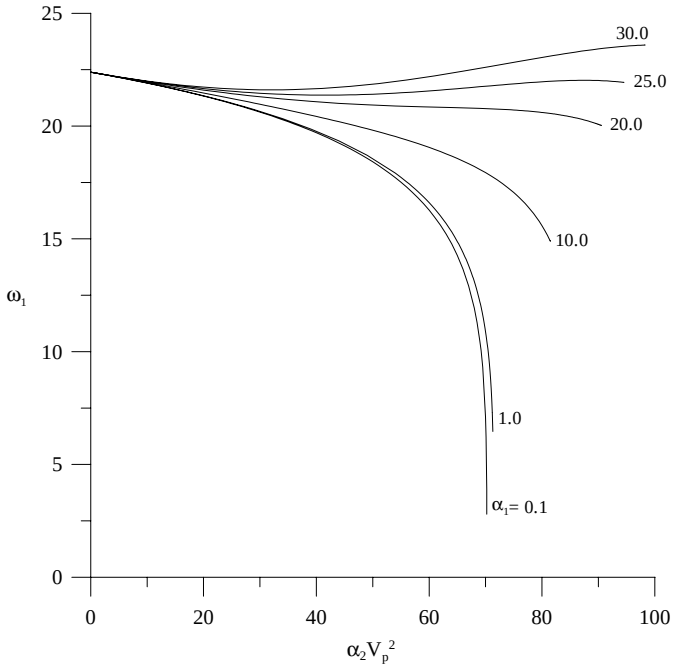

Figure 5.2: Variation of the fundamental natural frequency with $\alpha_2 V_p^2$ for various values of α_1 and no axial load.

Figure 5.3 shows variation the fundamental natural frequency with $\alpha_2 V_p^2$ for various values of N and $\alpha_1 = 3.7$. As the electrostatic force increases, the fundamental natural frequency decreases consistently and approaches zero as pull-in develops. Increasing the axial load from compressive values to tensile values increases the fundamental natural frequency for the same level of electrostatic forcing and increases the level of electrostatic forcing at pull-in.

Figures 5.4 and 5.5 show variation of the first four natural frequencies with $\alpha_2 V_p^2$. Increasing the value of either α_1 or N increases the level of electrostatic forcing at pull-in. In both figures, the effect of the electrostatic force in shifting the natural frequencies to lower values can be seen clearly in the fundamental natural frequency ω_1. As equation (3.13a) indicates, the coefficient of the mode shape ϕ_n is a function of both the electrostatic force and the natural frequency. Therefor, for higher modes, the contribution of the electrostatic force to the magnitude of the coefficient decreases leading to smaller shifts in the natural frequency. Further, in Figure 5.4, an upward

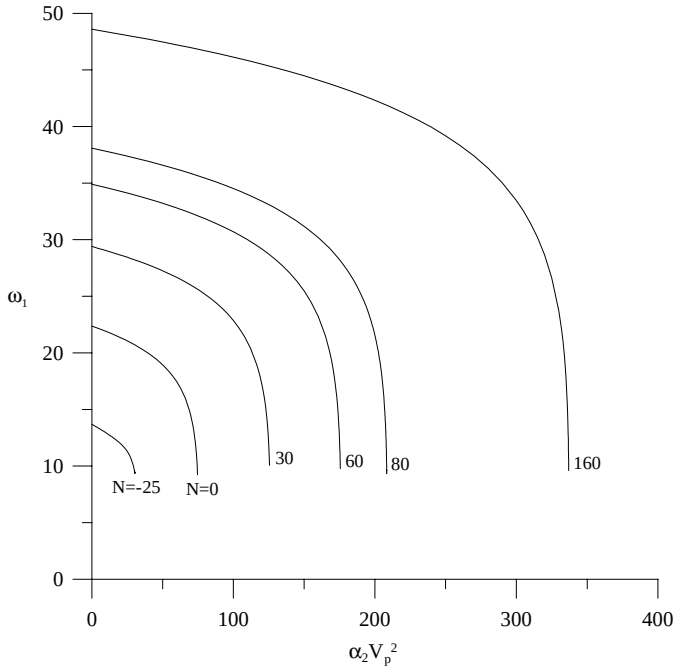

Figure 5.3: Variation of the fundamental natural frequency with $\alpha_2 V_p^2$ when $\alpha_1 = 3.7$ for various axial forces.

shift in the fourth natural frequency ω_4 is observed as the deflection increases due to the effect of mid-plane stretching.

5.2 Discussion

Taking the partial derivative of the static solution $w_s(x)$ in equations (3.9) with respect to $\xi = \alpha_2 V_p^2$, we obtain

$$\frac{\partial^5 w_s}{\partial x^4 \partial \xi} - (\alpha_1 \Gamma_1 + N)\frac{\partial^3 w_s}{\partial x^2 \partial \xi} - 2\alpha_1 \Gamma \left(w_s, \frac{\partial w_s}{\partial \xi} \right) \frac{\partial^2 w_s}{\partial x^2} - \frac{2\xi}{(1-w_s)^3}\frac{\partial w_s}{\partial \xi} = \frac{1}{(1-w_s)^2} \tag{5.1}$$

$$\frac{\partial w_s}{\partial \xi} = 0 \text{ and } \frac{\partial^2 w_s}{\partial x \partial \xi} = 0 \qquad \text{at} \qquad x = 0 \text{ and } x = 1 \tag{5.2}$$

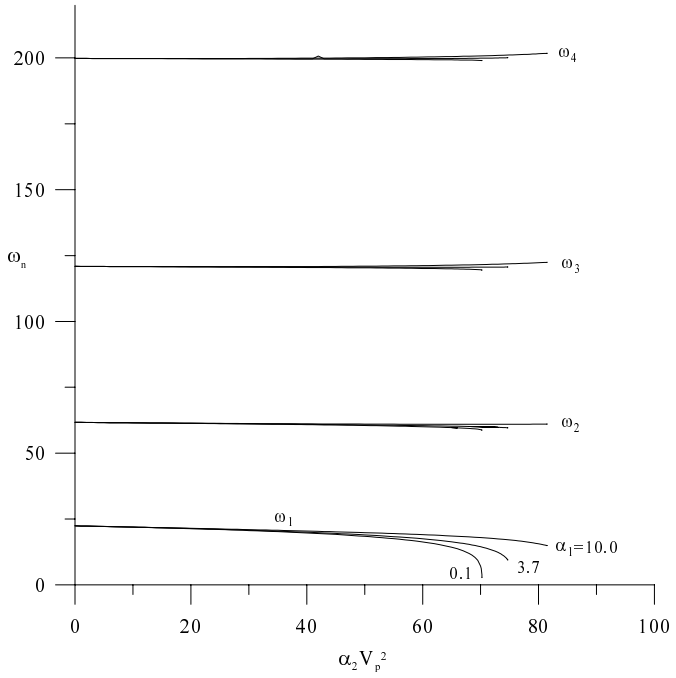

Figure 5.4: Variation of the first four natural frequencies of the microbeam with $\alpha_2 V_p^2$ for various values of α_1 and no axial load.

Defining a new variable $\zeta = \frac{\partial w_s}{\partial \xi}$, representing the slope of the curves in Figures 4.1 and 4.3, we rewrite equations (5.1) and (5.2) as

$$\frac{d^4\zeta}{dx^4} - (\alpha_1\Gamma_1 + N)\frac{d^2\zeta}{dx^2} - 2\alpha_1\Gamma\left(w_s, \zeta\right)\frac{d^2 w_s}{dx^2} - \frac{2\xi\zeta}{\left(1-w_s\right)^3} = \frac{1}{(1-w_s)^2} \tag{5.3}$$

$$\zeta = 0 \text{ and } \frac{d\zeta}{dx} = 0 \qquad \text{at} \qquad x = 0 \text{ and } x = 1 \tag{5.4}$$

The integral-differential operator $\mathcal{L}(\zeta)$in equation (5.3) is the same as $\mathcal{L}(\phi)$ in the eigenvalue problem, equation (3.13a). Since the fundamental natural frequency ω_1 is also one of the eigenvalues of equations (3.13), as $\omega_1 \to 0$ the solutions of equations (5.3) and (5.4) grow and become unbounded; that is $\zeta(x) \to \infty$. This establishes the equivalence of the static and dynamic definitions of the pull-in phenomenon: $\frac{\partial w_s}{\partial \xi} \to \infty \Rightarrow \omega_1 \to 0$.

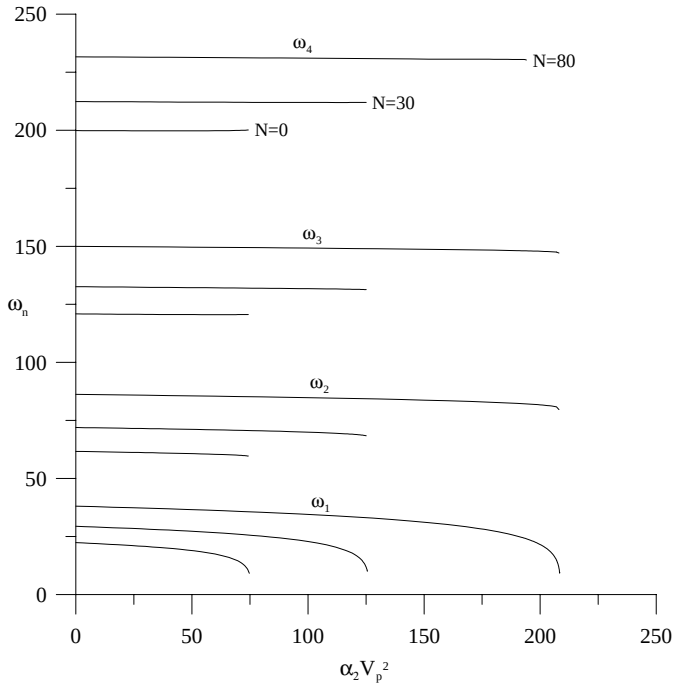

Figure 5.5: Variation of the first four natural frequencies with $\alpha_2 V_p^2$ for $\alpha_1 = 3.7$ and various applied axial loads.

Chapter 6

Nonlinear Response of Microbeams to a Combined DC and AC Electric Force

In this Chapter, we study the dynamic response of microbeams when actuated by electric loads composed of DC and AC components. Such cases exist in resonant microsensors.

First, we use the method of multiple scales to determine two nonlinear first-order ordinary-differential equations governing the amplitude and phase of the response to a primary resonance excitation of the first mode. We use these equations to derive the frequency-response equation and analyze the stability of the response. We also derive an equation that describes the nonlinear resonance frequency. We compare the results obtained using our model with the experimental results available in the literature. Then, we study the effect of the nondimensional design parameters N, α_1, and $\alpha_2 V_p^2$ on the normalized nonlinear resonance frequency $\frac{\Omega_r}{\omega}$.

Finally, we use the method of multiple scales to investigate the possibility of activating a three-to-one internal resonance between the first and second modes, which if exists can be very dangerous on the resonator.

6.1 Primary Resonance of the First Mode

6.1.1 Perturbation Analysis

We investigate the response of a microbeam to a primary resonance excitation of the first mode because it is the case used in resonator applications. However, the analysis is general and can be used to study the primary resonance of any mode.

There are at least two approaches for determining the response of a distributed-parameter system with quadratic and cubic nonlinearities to a primary resonance. In the first approach, one discretizes the governing integral-partial-differential equation and associated boundary conditions, keeps enough modes in the discretization, and uses a perturbation method to attack the discretized system [2]. In the second approach, called the direct approach, one attacks directly the distributed-parameter problem. In this Section, we attack equations (3.10) directly using the method of multiple scales [33] to determine a uniformly valid approximate solution. To this end, we seek a second-order uniform solution of equations (3.10) in the form

$$u(x,t;\epsilon) = \epsilon u_1(x,T_0,T_2) + \epsilon^2 u_2(x,T_0,T_2) + \epsilon^3 u_3(x,T_0,T_2) + \cdots \tag{6.1}$$

where ϵ is a small nondimensional bookkeeping parameter, $T_0 = t$, and $T_2 = \epsilon^2 t$. We note that $u(x,t)$ does not depend on $T_1 = \epsilon t$ because, as shown below, secular terms arise at $O(\epsilon^3)$. In order that the nonlinearity balances the effects of the damping and excitation, we scale them so that they appear together in the modulation equations as follows:

$c = \epsilon^2 c$, $v(t) = \epsilon^3 V_{AC}\cos(\Omega t)$

where V_{AC} is the magnitude of the applied AC voltage and Ω is the excitation frequency. Substituting equation (6.1) into equation (3.10a) and equating coefficients of like powers of ϵ, we obtain

order ϵ

$$\mathcal{L}(u_1) = D_0^2 u_1 + u_1^{iv} - \alpha_1\Gamma_1 u_1'' - N u_1'' - 2\alpha_1\Gamma\left(w_s, u_1\right) w_s'' - \frac{2\alpha_2 V_p^2}{\left(1-w_s\right)^3} u_1 = 0 \tag{6.2}$$

order ϵ^2

$$\mathcal{L}(u_2) = \alpha_1 w_s^{''} \Gamma(u_1, u_1) + 2\alpha_1 \Gamma(w_s, u_1)\, u_1^{''} + \frac{3\alpha_2 V_p^2}{(1-w_s)^4} u_1^2 \tag{6.3}$$

order ϵ^3

$$\begin{aligned}\mathcal{L}(u_3) = &-2D_0D_2u_1 - cD_0u_1 + 2\alpha_1 w_s^{''}\Gamma(u_1, u_2) + 2\alpha_1\Gamma(w_s, u_2)\, u_1^{''} + 2\alpha_1\Gamma(w_s, u_1)\, u_2^{''} \\ &+ \alpha_1\Gamma(u_1, u_1)\, u_1^{''} + 2\bar{F}(x)\cos(\Omega T_0) + \frac{6\alpha_2 V_p^2}{(1-w_s)^4} u_1 u_2 + \frac{4\alpha_2 V_p^2}{(1-w_s)^5} u_1^3\end{aligned} \tag{6.4}$$

where $\bar{F}(x) = \frac{\alpha_2 V_p V_{AC}}{(1-w_s)^2}$. The boundary conditions at all orders are given by

$$u_j = 0 \text{ and } u_j^{'} = 0 \quad \text{at } x = 0 \text{ and } x = 1, \quad j = 1, 2, 3 \tag{6.5}$$

The first-order problem given by equations (6.2) and (6.5) is identical to the linear eigenvalue problem, equations (3.11). Because in the presence of damping the homogeneous solutions corresponding to all modes that are not directly or indirectly excited decay with time [31], the solution of equations (6.2) and (6.5) is assumed to consist of only the directly excited mode. Accordingly, we express u_1 as

$$u_1 = A(T_2)e^{i\omega T_0}\phi(x) + \bar{A}(T_2)e^{-i\omega T_0}\phi(x) \tag{6.6}$$

where $A(T_2)$ is a complex-valued function that is determined by imposing the solvability condition at third order, the overbar denotes the complex conjugate, and ω and $\phi(x)$ are the natural frequency and corresponding eigenfunction of the considered mode, respectively. The eigenfunction $\phi(x)$ is normalized such that $\int_0^1 \phi^2 dx = 1$.

Substituting equation (6.6) into equation (6.3), we obtain

$$\mathcal{L}(u_2) = \left(A^2 e^{2\,i\omega T_0} + 2A\bar{A} + \bar{A}^2 e^{-2\,i\omega T_0}\right) h(x) \tag{6.7}$$

where

$$h(x) = \alpha_1 \Gamma(\phi, \phi)\, w_s'' + 2\alpha_1 \phi'' \Gamma(w_s, \phi) + \frac{3\alpha_2 V_p^2}{(1-w_s)^4}\phi^2$$

The solution of equations (6.7) and (6.5) can be expressed as

$$u_2 = \psi_1(x) A^2 e^{2i\omega T_0} + 2\psi_2(x) A\bar{A} + \psi_1(x)\bar{A}^2 e^{-2i\omega T_0} \tag{6.8}$$

where ψ_1 and ψ_2 are the solutions of the boundary-value problems

$$M(\psi_i, 2\omega\delta_{1i}) = h(x) \tag{6.9}$$

$$\psi_j = 0 \text{ and } \psi_j' = 0 \quad \text{at } x = 0 \text{ and } x = 1, \quad j = 1, 2 \tag{6.10}$$

and δ_{ij} is the Kronecker delta and the linear differential operator $M(\psi, \omega)$ is defined as

$$M(\psi, \omega) = \psi^{iv} - \omega^2\psi + \alpha_1\Gamma_1\psi'' - N\psi'' - 2\alpha_1\Gamma(w_s, \psi)\, w_s'' - \frac{2\alpha_2 V_p^2}{(1-w_s)^3}\psi \tag{6.11}$$

To describe the nearness of the excitation frequency Ω to the fundamental natural frequency ω, we introduce the detuning parameter σ defined by

$$\Omega = \omega + \epsilon^2\sigma \tag{6.12}$$

Substituting equations (6.6), (6.8), and (6.12) into equation (6.4) and keeping the terms that produce secular terms only, we obtain

$$\mathcal{L}(u_3) = \left[-i\omega\left(2A' + cA\right)\phi(x) + \chi(x)A^2\bar{A} + \bar{F}(x)e^{i\sigma T_2}\right] e^{i\omega T_0} + \text{cc} + \text{NST} \tag{6.13}$$

where A' denotes the derivative of A with respect to T_2, cc denotes the complex conjugate of the preceding terms, and NST stands for terms that do not produce

secular terms. The function $\chi(x)$ is defined as

$$\chi(x) = \chi_q^G(x) + \chi_c^G(x) + \chi_q^E(x) + \chi_c^E(x)$$

where

$$\begin{aligned}
\chi_q^G(x) &= 2\alpha_1 w_s'' \Gamma(\psi_1, \phi) + 4\alpha_1 w_s'' \Gamma(\psi_2, \phi) + \left(2\alpha_1 \psi_1'' + 4\alpha_1 \psi_2''\right) \Gamma(w_s, \phi) \\
&\quad + 2\phi'' \alpha_1 \Gamma(w_s, \psi_1) + 4\phi'' \alpha_1 \Gamma(w_s, \psi_2) \\
\chi_c^G(x) &= 3\phi'' \alpha_1 \Gamma(\phi, \phi) \\
\chi_q^E(x) &= \frac{6\alpha_2 V_p^2}{(1-w_s)^4} \left(2\phi\psi_2 + \phi\psi_1\right) \\
\chi_c^E(x) &= \frac{4\alpha_2 V_p^2}{(1-w_s)^5} \phi^3
\end{aligned}$$

The subscripts q and c denote quadratic and cubic nonlinear terms and the superscripts G and E denote terms produced by the geometric and electric nonlinearities.

At the third-order approximation, we do not need to solve for u_3 because we approximate u by a second-order expansion. Only, we need to impose the solvability condition [33] on equations (6.13) and (6.5) to derive an equation for the function A. Because the homogeneous problem governing u_3 has a nontrivial solution, the corresponding nonhomogeneous problem has a solution only if the right-hand side of equation (6.13) is orthogonal to every solution of the adjoint homogeneous problem governing u_3 [33]. We note that our problem is self adjoint, the adjoints are given by $\phi(x)e^{\pm i\omega T_0}$. Multiplying the right-hand side of equation (6.13) with $\phi(x)e^{-i\omega T_0}$ and integrating the result from $x = 0$ to $x = 1$, we obtain the following solvability condition:

$$2i\omega(D_2 A + \mu A) + 8SA^2\bar{A} - Fe^{i\sigma T_2} = 0 \tag{6.14}$$

where

$$
\begin{aligned}
S &= S_q^G + S_c^G + S_q^E + S_c^E \\
S_q^G &= -\frac{1}{8}\int_0^1 \chi_q^G \phi dx \\
S_c^G &= -\frac{1}{8}\int_0^1 \chi_c^G \phi dx \\
S_q^E &= -\frac{1}{8}\int_0^1 \chi_q^E \phi dx \\
S_c^E &= -\frac{1}{8}\int_0^1 \chi_c^E \phi dx \\
\mu &= \frac{1}{2}\int_0^1 c\phi^2 dx \\
F &= \int_0^1 \bar{F}\phi dx
\end{aligned}
$$

Here, S is the effective nonlinear coefficient of the system and S_n^m denotes a nonlinear coefficient of source m (electric or geometric) and of order n (quadratic or cubic).

Next, we express A in the polar form $A = \frac{1}{2}ae^{i\beta}$, where a and β are real-valued functions, representing, respectively, the amplitude and phase of the response. Substituting for A in equation (6.14), separating the real and imaginary parts, and letting $\gamma = \sigma T_2 - \beta$, we obtain the following modulation equations:

$$a' = -\mu a + \frac{F}{\omega}\sin\gamma \tag{6.15}$$

$$a\gamma' = a\sigma - \frac{Sa^3}{\omega} + \frac{F}{\omega}\cos\gamma \tag{6.16}$$

Substituting equations (6.6) and (6.8) into equation (6.1) and setting $\epsilon = 1$, we express, to the second approximation, the microbeam response to the external excitation as

$$u(x,t) = a\cos(\Omega t - \gamma)\phi(x) + \frac{1}{2}a^2\left[\psi_2(x) + \cos 2(\Omega t - \gamma)\psi_1(x)\right] + \cdots \tag{6.17}$$

where a and γ are governed by equations (6.15) and (6.16).

It follows from equation (6.17) that periodic solutions of equations (3.10) correspond to constant a and γ; that is, the fixed points (a_0, γ_0) of equations (6.15) and

(6.16). Thus, letting $a' = \gamma' = 0$ in equations (6.15) and (6.16) and eliminating γ_0 from the resulting equations, we obtain the following frequency-response equation:

$$a_0^2 \left[\mu^2 + \left(\sigma - \frac{S a_0^2}{\omega} \right)^2 \right] = \frac{F^2}{\omega^2} \tag{6.18}$$

Equation (6.18) is an implicit equation for the amplitude a of the periodic response as a function of the detuning parameter σ (which is a representation of the excitation frequency), the effective nonlinear coefficient S, the damping coefficient μ, and the amplitude of excitation F. Solving equation (6.18) for σ, we obtain

$$\sigma = \pm \frac{1}{a_0} \left[\frac{F^2}{\omega^2} - \mu^2 a_0^2 \right]^{\frac{1}{2}} + \frac{S a_0^2}{\omega} \tag{6.19}$$

Recalling that $\sigma = \Omega - \epsilon^2 \omega$, setting $\epsilon = 1$, and noting that the amplitude a is maximum when the expression inside the square root vanishes, we obtain the following equation for the nonlinear resonance frequency:

$$\Omega_r = \omega + \frac{S F^2}{\omega^3 \mu^2} \tag{6.20}$$

The parameters μ is related to the quality factor Q by

$$\mu = \frac{\omega}{2Q} \tag{6.21}$$

Substituting equation (6.21) into equation (6.20), we obtain

$$\Omega_r = \omega + \frac{4SQ^2}{\omega^5} F^2 \tag{6.22}$$

Equation (6.22) relates the nonlinear resonance frequency Ω_r to the effective nonlinearity S of the system, the amplitude F of the AC forcing, and the quality factor Q.

The stability of the fixed points (a_0, γ_0) is determined by examining the eigenvalues of the Jacobian matrix of equations (6.15) and (6.16) evaluated at the corresponding

fixed point [34]. The characteristic equation is

$$\lambda^2 + 2\mu\lambda + \left[\mu^2 + (\sigma - \frac{3Sa_0^2}{\omega})(\sigma - \frac{Sa_0^2}{\omega})\right] = 0 \tag{6.23}$$

For asymptotically stable solutions, all of the real parts of the eigenvalues must be negative.

6.1.2 Results

To describe the dynamic response of the microbeam, we need to determine the natural frequency ω, the excitation amplitude F, the effective nonlinearity of the system S, and the damping coefficient μ or Q.

As a first step, we solved the boundary-value problem, equations (3.9), for the deflection due to the electrostatic force. We did this iteratively using a shooting method to determine the value of the integral $\Gamma(w_s, w_s)$. Using the converged solution w_s, we solved the boundary-value problem, equations (3.13), for the fundamental natural frequency and its corresponding eigenfunction. We used a shooting method to iterate on Γ_2, ω, and ϕ until they converged to predefined tolerances. Next, we solved the boundary-value problems, equations (6.9)-(6.11), to evaluate the functions ψ_1 and ψ_2 using a method similar to that used to solve equations (3.13). Finally, we evaluated the χ_i^j, S, and F.

We begin by comparing the results obtained by the perturbation analysis using the present model with the experimental results of Tilmans and Legtenburg [7] and Gui et al. [10]. Results from other papers, which are mentioned in the Introduction, are not used because either they were produced from another device configuration [12,13], for which our model does not apply, or the authors did not give enough data about the specifications of their devices [5,11].

In Figure 6.1, we compare the normalized nonlinear resonance frequency $\frac{\Omega_r}{\omega}$ obtained using equation (6.22) with those obtained theoretically and experimentally by Tilmans and Legtenburg [7] for two microbeams of lengths $210\mu m$ and $310\mu m$ with $h = 1.5\mu m$, $b = 100\mu m$, $d = 1.18\mu m$, and subject to an axial load of $0.0009\ N$. The

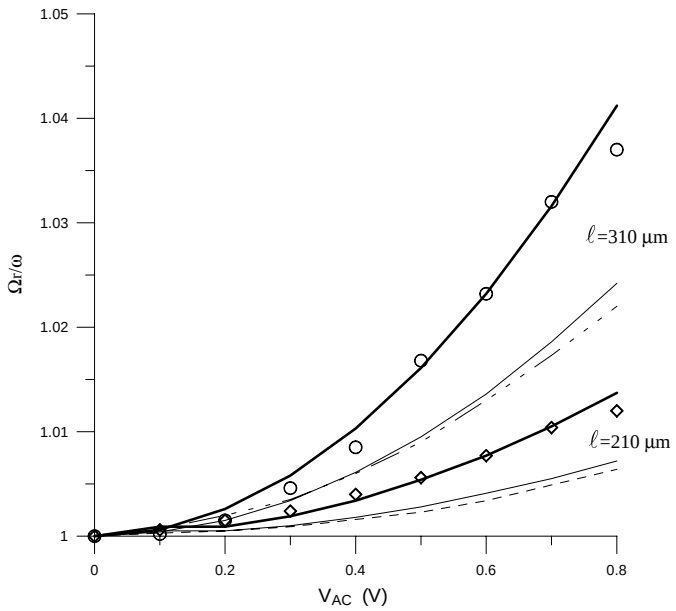

Figure 6.1: Comparison of the normalized nonlinear resonance frequency $\frac{\Omega_r}{\omega}$ calculated using our model (solid lines) with those obtained theoretically (dashed lines) and experimentally by Tilmans and Legtenburg [7] for two microbeams of lengths $210\mu m$ (diamonds) and $310\mu m$ (circles). The thin solid lines are based on the quality factors of Tilmans and Legtenburg [7] and the thick solid lines are based on quality factors estimated using our model.

DC polarization voltage $V_p = 1\ V$ for data points of the first microbeam except for the first two points where $V_p = 2\ V$. For the second microbeam, $V_p = 2\ V$ for all data points. The theory of Tilmans and Legtenburg [7] is based on Rayleigh's energy method modified to account for electric forces and mid-plane stretching. The latter effect however was misrepresented, as we show in Appendix A.

We show two sets of calculated results for each microbeam obtained using equation (6.22). The first set, shown as thin solid lines, uses the same values of Q of Tilmans and Legtenburg [7]. They extracted the values of Q analytically using an equation derived from their model. The parameters of this model were obtained by fitting the predicted frequency-response curve at a low DC voltage to the one obtained experimentally. These quality factors are Q=592 and 151 for the $210\mu m$ and $310\mu m$ microbeams, respectively. As shown in Figure 6.1, these values give poor results. Legtenburg and Tilmans [27] mentioned that the quality factor for the design of their device varies

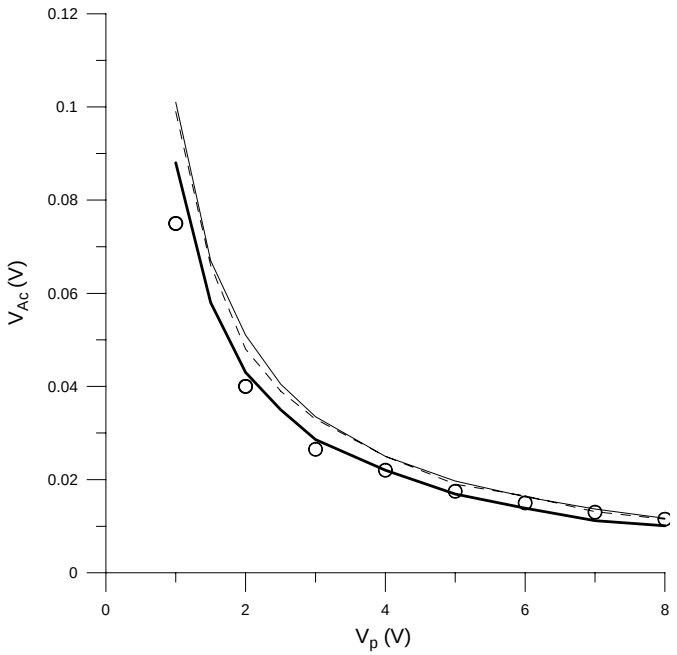

Figure 6.2: Comparison of the hysteretic points obtained using our model (solid lines) with those obtained theoretically (dashed line) and experimentally (circles) by Gui et al. [10]. The thin solid line is based on the quality factor $Q = 900$ reported by Gui et al. and the thick solid line is based on a quality factor $Q = 1000$ estimated using our model.

across the wafer due to variations in the sealing pressure of the microbeam encapsulation. Because such variations can lead to a wrong measurement of Q and due to the difficulty of measuring the system damping, in general, we determined the quality factors by matching $\frac{\Omega_r}{\omega}$ obtained using equation (6.22) at $V_{AC} = 0.6\ V$ to the experimental value of Tilmans and Legtenburg [7]. We obtained Q=816.6 and 197 for the $210\mu m$ and $310\mu m$ microbeams, respectively. The results obtained using these values, shown as thick solid lines, are in excellent agreement with the experimental results.

In Figure 6.2, we show another comparison for the hysteretic points (points where the microbeam response becomes multi-valued) predicted by our model with those obtained theoretically and experimentally by Gui et al. [10] for a microbeam of length $210\mu m$ and $h = 1.5\mu m$, $b = 100\mu m$, $d = 1\mu m$, and Q=900. The theoretical results of Gui et al. [10] were obtained using a modified Rayleigh's energy method that accounts for mid-plane stretching and electric forces. Mid-plane stretching however

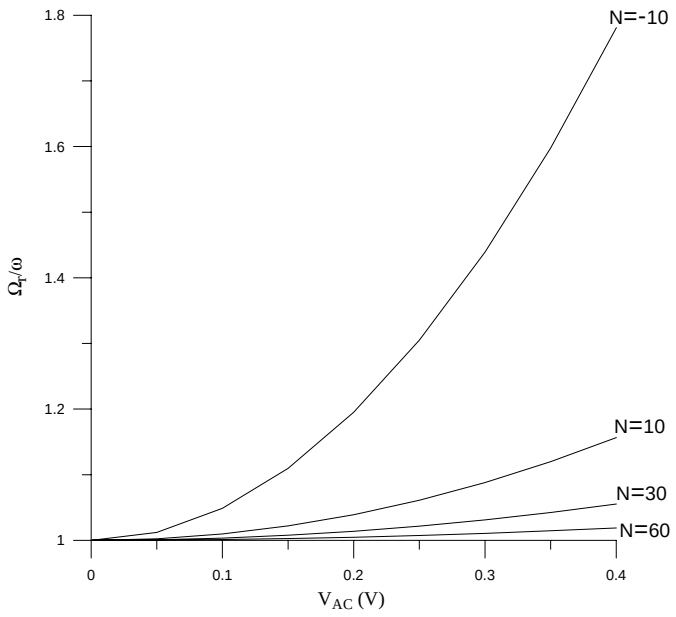

Figure 6.3: Variation of the normalized nonlinear resonance frequency $\frac{\Omega_r}{\omega}$ with V_{AC} for various values of the nondimensional axial load N. The values of α_1, $\alpha_2 V_p^2$, and Q are 3.7, 5.5, and 796, respectively.

was misrepresented, as we show in Appendix A.

In Figure 6.2, we show also two curves obtained using our theory corresponding to two different values of Q: the thick solid line was obtained using Q=1000, which was determined by matching our result at $V_p = 4\ V$ to the experimental result of Gui et al. [10]. The thin solid line was obtained using Q=900, which is the value used by Gui et al. [10]. We estimated the axial force of $\hat{N} = 0.00011N$ by fitting the theoretically obtained natural frequency to the experimental value obtained by Gui et al. [10]. There is excellent agreement between our results and the experimental results.

Next, we study the effect of the nondimensional design parameters on the nonlinear resonance frequency. As indicated by equation (6.22), the nondimensional design parameters affect the nonlinear resonance frequency in two ways: the first is by changing the effective nonlinearity of the system S. The second is by changing the fundamental natural frequency ω.

In Figure 6.3, we show the effect of varying the driving voltage AC on $\frac{\Omega_r}{\omega}$ for various

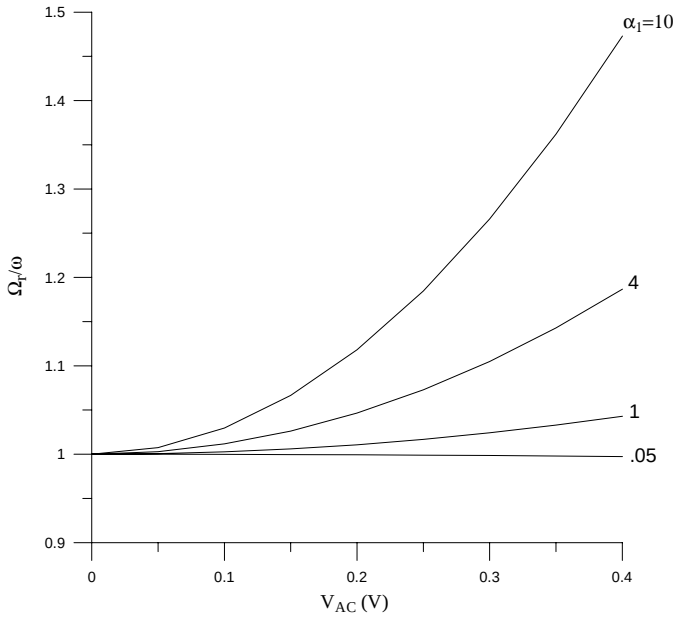

Figure 6.4: Variation of the normalized nonlinear resonance frequency $\frac{\Omega_r}{\omega}$ with V_{AC} for various values of α_1. The values of N, $\alpha_2 V_p^2$, and Q are 8.7, 5.5, and 796, respectively.

values of the nondimensional axial load N. Increasing the driving voltage amplitude AC increases $\frac{\Omega_r}{\omega}$. On the other hand, increasing the axial force N at a constant V_{AC} decreases $\frac{\Omega_r}{\omega}$ and also increases its linear behavior. We note that negative values of N, which correspond to compressive loads, have a greater effect on $\frac{\Omega_r}{\omega}$.

In Figures 6.4, we show the effect of varying the driving voltage amplitude AC on $\frac{\Omega_r}{\omega}$ for various values of α_1. It can be seen that, for values of α_1 greater than 0.05, increasing AC increases $\frac{\Omega_r}{\omega}$. In contrast, for values of α_1 less than 0.05, increasing AC leads to a decrease in $\frac{\Omega_r}{\omega}$. We also note that increasing α_1 increases the nonlinear behavior of $\frac{\Omega_r}{\omega}$ and its value at a constant value of AC.

In Figures 6.5, we show the effect of varying AC on $\frac{\Omega_r}{\omega}$ for various values of $\alpha_2 V_p^2$. Increasing $\alpha_2 V_p^2$ at a constant V_{AC} increases $\frac{\Omega_r}{\omega}$ up to a value of $\alpha_2 V_p^2 \simeq 50$. Above this value, the increase in $\frac{\Omega_r}{\omega}$ becomes smaller until it is reversed completely at $\alpha_2 V_p^2 \simeq 60$, where the nonlinear resonance frequency becomes highly sensitive to changes in the DC polarization voltage. In fact, a slight increase in $\alpha_2 V_p^2$ beyond this value leads to a sharp drop, which can even reach zero, in the nonlinear resonance frequency

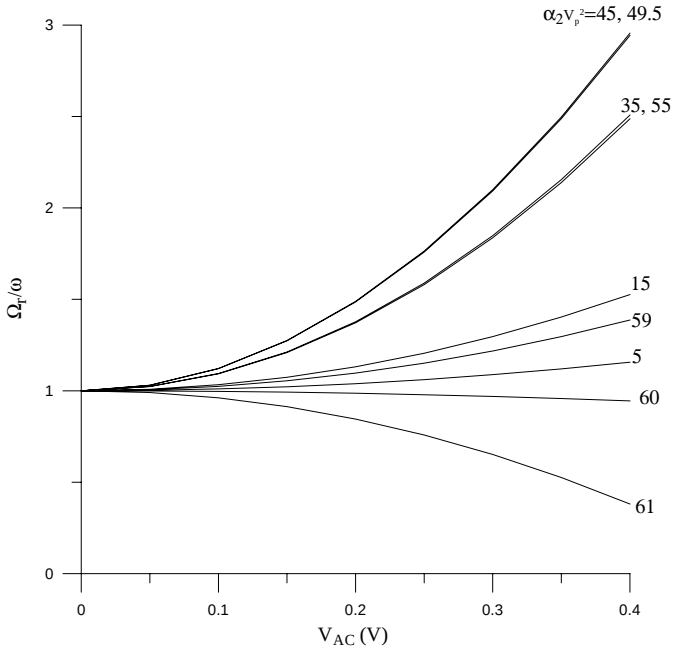

Figure 6.5: Variation of the normalized nonlinear resonance frequency $\frac{\Omega_r}{\omega}$ with V_{AC} for various values of $\alpha_2 V_p^2$. The values of α_1, N, and Q are 3.7, 8.7, and 796, respectively.

with increasing V_{AC}. We note that such a strange behavior occurs before reaching the pull-in limit, which in this case occurs at $\alpha_2 V_p^2 \simeq 90$. This result shows that the nondimensional parameter $\alpha_2 V_p^2$ changes the dynamic response of the microbeam from a hardening to a softening response. This is because, for this range of $\alpha_2 V_p^2$, the electrostatic force, which tends to lower the resonance frequency, drastically dominates the mid-plane stretching, which tends to increase the resonance frequency.

6.1.3 Discussion

In order to better understand how the nondimensional parameters N, α_1, and $\alpha_2 V_p^2$ affect the effective nonlinearity of the system, we study the influence of each parameter on the nonlinear coefficients S_q^G, S_c^G, S_q^E, S_c^E, and S

In Figure 6.6, we show variation of the nonlinear coefficients with increasing the axial load N. It shows that increasing N in the positive range leads only to a slight linear decrease in the mid-plane stretching represented by S_c^G, and hence in the effective nonlinear coefficient S. However, this is not the factor that leads to the decrease in $\frac{\Omega_r}{\omega}$

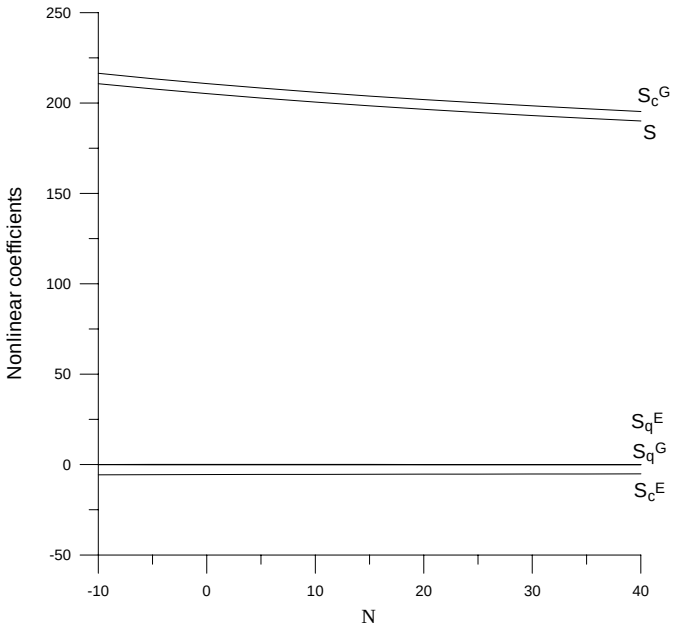

Figure 6.6: Variation of the nonlinear coefficients with the axial load N. The values of α_1 and $\alpha_2 V_p^2$ are 3.7 and 5.5, respectively.

with increasing N that is shown in Figure 6.3. Increasing N also increases ω, which according to equation (6.22), decreases the shift in $\frac{\Omega_r}{\omega}$. This agrees with the results of Figure 6.3, where at large N the ratio $\frac{\Omega_r}{\omega}$ approaches unity.

In Figure 6.7, we show variation of the nonlinear coefficients with α_1. Increasing α_1 increases linearly the mid-plane stretching coefficient S_c^G, without affecting the other nonlinear coefficients. The increase in S_c^G, and so in S, increases $\frac{\Omega_r}{\omega}$, as indicated by equation (6.22). On the other hand, increasing α_1 increases ω, which tends to decrease $\frac{\Omega_r}{\omega}$. The effect of increasing S however dominates the later effect. This explains the increase in the normalized nonlinear resonance frequency with increasing α_1 at a constant V_{AC}, which is seen in Figure 6.4. The effective nonlinear coefficient S starts with a negative value for very small values of α_1, which explains the qualitative change observed in Figure 6.4 near this range of values.

In Figure 6.8, we show variation of the nonlinear coefficients with $\alpha_2 V_p^2$. For small values of $\alpha_2 V_p^2$, the effective nonlinear coefficient S varies slightly with increasing $\alpha_2 V_p^2$ up to values near 55 where the quadratic electric term S_c^E starts to decrease

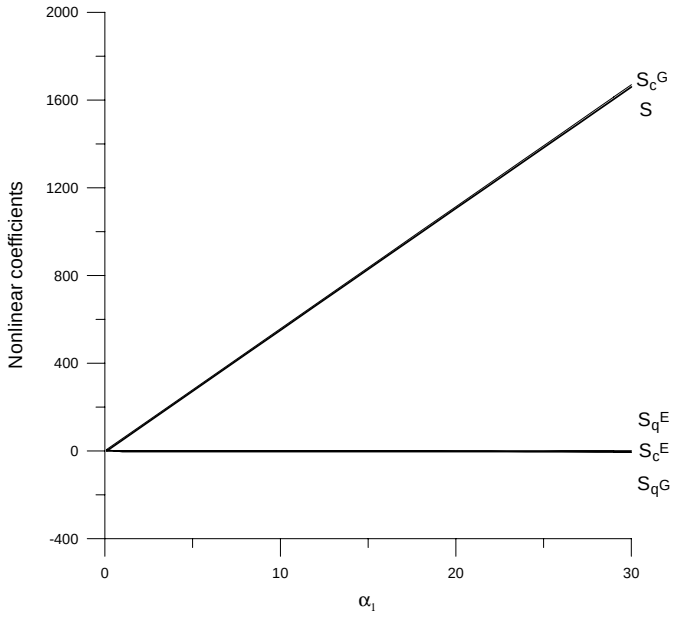

Figure 6.7: Variation of the nonlinear coefficients with α_1. The values of N and $\alpha_2 V_p^2$ are 8.7 and 5.5, respectively.

sharply, thereby dominating all other nonlinear coefficients. At $\alpha_2 V_p^2 \simeq 60$, the sign of S changes from positive, corresponding to a hardening behavior, to negative, corresponding to a softening behavior, which explains the qualitative change in the dynamic behavior observed in Figure 6.5. This is a significant result; it shows that using a spring-mass model with a cubic nonlinearity, which is the model usually used in the literature, is inaccurate and might lead to wrong results. Such models neglect the quadratic nonlinearity, which is due to the electrostatic force and the static deflection. As clearly shown in Figure 6.8, this nonlinearity becomes dominant and governs the dynamic behavior beyond a critical value of $\alpha_2 V_p^2$. Further, we note that assuming a single value for the effective nonlinearity in the model may introduce another source of error because, as shown in Figure 6.8, the effective nonlinearity is a strong function of the electrostatic force.

We note that the DC voltage needed to achieve a linear behavior in the nonlinear resonance frequency (corresponding to $S = 0$) is relatively high and may not be attainable in resonant sensor applications. This result is in agreement with that found

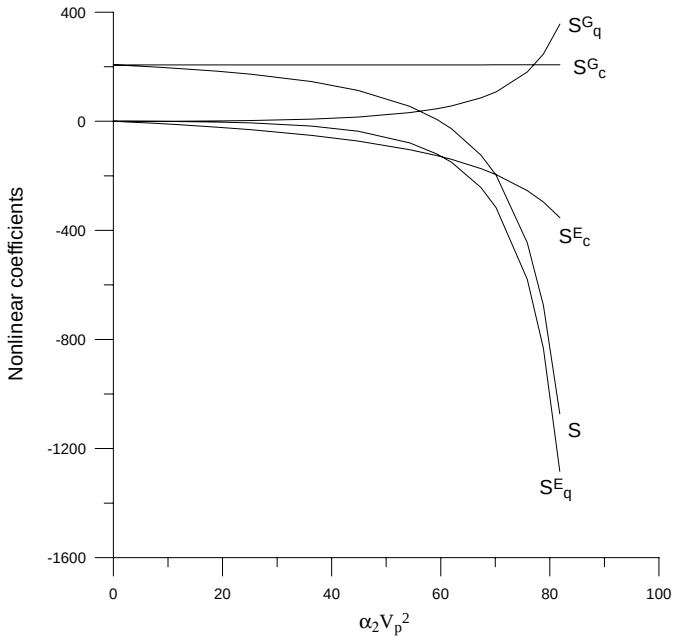

Figure 6.8: Variation of the nonlinear coefficients with $\alpha_2 V_p^2$. The values of α_1 and N are 3.7 and 8.7, respectively.

by Turner and Andrews [11].

6.2 Three-to-one Internal Resonance

6.2.1 Perturbation Analysis

We study the possibility of activating a nonlinear modal interaction or modal coupling between the first and second modes when the first mode is excited with a primary resonance. For some system parameters, the frequency of the first mode is close to one-third the frequency of the second mode, suggesting the possibility of activating a three-to-one internal resonance between them. Such a resonance, if activated, can lead to complex behaviors that may affect the performance of the device.

We apply the method of multiple scales directly to equations (3.10). The analysis presented here is general and applicable to any two modes whose frequencies are in the ratio of three-to-one. We seek a solution of equations (3.10) in the form of equation (6.1) and obtain equations (6.2)-(6.5). Because in the presence of damping all modes

that are not directly or indirectly excited decay with time [31], the solution of equations (6.2) and (6.5) is assumed to consist of the two interacting modes; that is,

$$u_1 = A_n(T_2)e^{i\omega_n T_0}\phi_n(x) + A_m(T_2)e^{i\omega_m T_0}\phi_m(x) + \text{cc} \tag{6.24}$$

where m and n denote the two modes being considered and the ϕ_j are normalized such that $\int_0^1 \phi_j^2 dx = 1$. Substituting equation (6.24) into equation (6.3) yields

$$\begin{aligned}\mathcal{L}(u_2) =& A_n^2 e^{2i\omega_n T_0}h_{1n}(x) + A_m^2 e^{2i\omega_m T_0}h_{1m}(x) + A_n\bar{A}_n h_{1n}(x) + A_m\bar{A}_m h_{1m}(x) \\ &+ \left(A_n A_m e^{i(\omega_n+\omega_m)T_0} + A_n\bar{A}_m e^{i(\omega_n-\omega_m)T_0}\right)H_{nm}(x) + \text{cc}\end{aligned} \tag{6.25}$$

where

$h_{1i}(x) = \alpha_1\Gamma\left(\phi_i,\phi_i\right)w_s'' + 2\alpha_1\phi_i''\Gamma(w_s,\phi_i) + \frac{3\alpha_2 V_p^2}{(1-w_s)^4}\phi_i^2$

$H_{ij}(x) = 2\alpha_1\Gamma\left(\phi_i,\phi_j\right)w_s'' + 4\alpha_1\phi_i''\Gamma(w_s,\phi_j) + \frac{6\alpha_2 V_p^2}{(1-w_s)^4}\phi_i\phi_j$

and the functional Γ is defined in equation (3.6c).

We express the solution of equations (6.25) and (6.5) as

$$\begin{aligned}u_2 =& \psi_{1n}(x)A_n^2 e^{2i\omega_n T_0} + \psi_{1m}(x)A_m^2 e^{2i\omega_m T_0} + \psi_3(x)A_n A_m e^{i(\omega_n+\omega_m)T_0} + \\ &\psi_4(x)A_n\bar{A}_m e^{i(\omega_n-\omega_m)T_0} + \psi_{2n}(x)A_n\bar{A}_n + \psi_{2m}(x)A_m\bar{A}_m + \text{cc}\end{aligned} \tag{6.26}$$

where the ψ_j and ψ_{ij} are the solutions of the boundary-value problems

$$M(\psi_{1i}, 2\omega_i) = h_{1i}(x) \tag{6.27a}$$

$$M(\psi_{2i}, 0) = h_{1i}(x) \tag{6.27b}$$

$$M(\psi_3, \omega_n + \omega_m) = H_{nm}(x) \tag{6.27c}$$

$$M(\psi_4, \omega_n - \omega_m) = H_{nm}(x) \tag{6.27d}$$

The operator $M(\psi,\omega)$ is defined in equation (6.11). The boundary conditions for the ψ_j and ψ_{ij} are

$$\psi = 0 \text{ and } \psi' = 0 \quad \text{at } x = 0 \text{ and } x = 1 \tag{6.28}$$

Substituting equations (6.24) and (6.26) into equation (6.4) and considering the case $\omega_n \approx 3\omega_m$ and either $\Omega \approx \omega_n$ or ω_m, we obtain

$$\begin{aligned}\mathcal{L}(u_3) = &\left[-i\omega_n\left(2A_n' + cA_n\right)\phi_n(x) + \chi_{1n}(x)A_n^2\bar{A}_n + \chi_{nm}(x)A_nA_m\bar{A}_m\right]e^{i\omega_nT_0}\\ &+\left[-i\omega_m\left(2A_m' + cA_m\right)\phi_m(x) + \chi_{1m}(x)A_m^2\bar{A}_m + \chi_{MN}(x)A_mA_n\bar{A}_n\right]e^{i\omega_mT_0}\\ &+\chi_5A_m^3e^{3i\omega_mT_0} + \chi_6A_n\bar{A}_m^2e^{i(\omega_n-2\omega_m)T_0} + \bar{F}(x)e^{i\Omega T_0} + \text{cc} + \text{NST}\end{aligned} \tag{6.29}$$

where A_j' is the derivative of A_j with respect to T_2 and

$$\begin{aligned}\chi_{1i} = &2\alpha_1\Gamma(\psi_{1i},\phi_i)w_s'' + 4\alpha_1\Gamma(\psi_{2i},\phi_i)w_s'' + 2\alpha_1\Gamma(w_s,\psi_{1i})\phi_i'' + 4\alpha_1\Gamma(w_s,\psi_{2i})\phi_i''\\ &+3\alpha_1\Gamma(\phi_i,\phi_i)\phi_i'' + 2\alpha_1\Gamma(w_s,\phi_i)\psi_{1i}'' + 4\alpha_1\Gamma(w_s,\phi_i)\psi_{2i}'' + \frac{12\alpha_2V_p^2}{(1-w_s)^5}\phi_i^3\\ &+\frac{6\alpha_2V_p^2}{(1-w_s)^4}\left(\psi_{ii}\phi_i + \psi_{2i}\phi_i\right)\end{aligned}$$

$$\begin{aligned}\chi_{ij} = &2\alpha_1\Gamma(\psi_3,\phi_j)w_s'' + 2\alpha_1\Gamma(\psi_4,\phi_j)w_s'' + 4\alpha_1\Gamma(\phi_i,\psi_{2j}w_s'' + 2\alpha_1\Gamma(w_s,\psi_3)\phi_j''\\ &+2\alpha_1\Gamma(w_s,\psi_4)\phi_j'' + 4\alpha_1\Gamma(w_s,\psi_{2j})\phi_i'' + 2\alpha_1\Gamma(w_s,\phi_j)\psi_3'' + 2\alpha_1\Gamma(w_s,\phi_j)\psi_4''\\ &+4\alpha_1\Gamma(w_s,\phi_i)\psi_{2j}'') + 2\alpha_1\Gamma(\phi_j,\phi_j)\phi_i'' + 4\alpha_1\Gamma(\phi_i,\phi_j)\phi_j'' + \frac{24\alpha_2V_p^2}{(1-w_s)^5}\phi_i\phi_j^2\\ &+\frac{6\alpha_2V_p^2}{(1-w_s)^4}\left(\psi_3\phi_j + \psi_4\phi_j + 2\psi_{2j}\phi_i\right)\end{aligned}$$

$$\begin{aligned}\chi_5 = &2\alpha_1\Gamma(\psi_{1m},\phi_m)w_s'' + 2\alpha_1\Gamma(\psi_{1m},w_s)\phi_m'' + 2\alpha_1\Gamma(w_s,\phi_m)\psi_{1m}'' + \alpha_1\Gamma(\phi_m,\phi_m)\phi_m''\\ &+\frac{6\alpha_2V_p^2}{(1-w_s)^4}\psi_{1m}\phi_m\end{aligned}$$

$$\begin{aligned}\chi_6 = &2\alpha_1\Gamma(\psi_4,\phi_m)w_s'' + 2\alpha_1\Gamma(\psi_{1m},\phi_n)w_s'' + 2\alpha_1\Gamma(\psi_4,w_s)\phi_m'' + 2\alpha_1\Gamma(\psi_{1m},w_s)\phi_n''\\ &+2\alpha_1\Gamma(w_s,\phi_m)\psi_4'' + 2\alpha_1\Gamma(\phi_n,w_s)\psi_{1m}'' + +\alpha_1\Gamma(\phi_m,\phi_m)\phi_n'' + 2\alpha_1\Gamma(\phi_n,\phi_m)\phi_m''\\ &+\frac{6\alpha_2V_p^2}{(1-w_s)^4}\psi_4\phi_m + \frac{6\alpha_2V_p^2}{(1-w_s)^4}\psi_{1m}\phi_n + \frac{12\alpha_2V_p^2}{(1-w_s)^5}\phi_n\phi_m^2\end{aligned}$$

To describe the nearness of ω_n to $3\omega_m$ and Ω to either ω_n or ω_m, we introduce the detuning parameters σ_1 and σ_2 defined by

$$\omega_n = 3\omega_m + \epsilon^2\sigma_1 \text{ and } \Omega = \omega_i + \epsilon^2\sigma_2 \tag{6.30}$$

Because the homogeneous part of equations (6.29) and (6.5) has a nontrivial solution, the nonhomogeneous problem has a solution only if the right-hand side of equation (6.29) is orthogonal to every solution of the adjoint homogeneous problem governing u_3 [33]. We note that the problem is self-adjoint, and hence the adjoints are given by $\phi_j(x)e^{\pm i\omega_j T_0}$. Multiplying the right-hand side of equation (6.29) by $\phi_n(x)e^{-i\omega_n T_0}$ and $\phi_m(x)e^{-i\omega_m T_0}$, respectively, integrating the results from $x = 0$ to $x = 1$, and using equations (6.30), we obtain the following solvability conditions:

$$\begin{aligned} 2i\omega_n(D_2A_n + \mu_n A_n) = {} & 8S_{nn}A_n^2\bar{A}_n + 8S_{nm}A_nA_m\bar{A}_m + 8\Lambda_n A_m^3 e^{-i\sigma_1 T_2} \\ & + f_n(x)\delta_{in}e^{i\sigma_2 T_2} \end{aligned} \tag{6.31}$$

$$\begin{aligned} 2i\omega_m(D_2A_m + \mu_m A_m) = {} & 8S_{mm}A_m^2\bar{A}_m + 8S_{mn}A_mA_n\bar{A}_n + 8\Lambda_m A_n\bar{A}_m^2 e^{i\sigma_1 T_2} \\ & + f_m(x)\delta_{im}e^{i\sigma_2 T_2} \end{aligned} \tag{6.32}$$

where

$$\begin{aligned} \mu_i &= \frac{1}{2}\int_0^1 c\phi_i^2 dx \\ f_i &= \int_0^1 \bar{F}\phi_i dx \\ S_{ii} &= \frac{1}{8}\int_o^1 \chi_{1i}\phi_i dx, \;\; S_{ij} = \frac{1}{8}\int_o^1 \chi_{ij}\phi_i dx, \;\; i \neq j \\ \Lambda_n &= \frac{1}{8}\int_o^1 \chi_5\phi_n dx, \;\; \Lambda_m = \frac{1}{8}\int_o^1 \chi_6\phi_m dx \end{aligned}$$

The S_{ij} are nonlinear coefficients due to electric and geometric sources, and the Λ_i are the nonlinear interaction coefficients between the nth and mth modes.

Expressing the A_i in polar form and separating real and imaginary parts in equa-

tions (6.31) and (6.32), we obtain the modulation equations

$$a_n' = -\mu_n a_n - \frac{\Lambda_n a_m^3}{\omega_n}\sin\gamma_1 + \frac{f_n\delta_{in}}{\omega_n}\sin\gamma_2 \tag{6.33}$$

$$a_n\beta_n' = -\frac{S_{nn}a_n^3}{\omega_n} - \frac{S_{nm}a_n a_m^2}{\omega_n} - \frac{\Lambda_n a_m^3}{\omega_n}\cos\gamma_1 - \frac{f_n\delta_{in}}{\omega_n}\cos\gamma_2 \tag{6.34}$$

$$a_m' = -\mu_m a_m - \frac{\Lambda_m a_n a_m^2}{\omega_m}\sin\gamma_1 + \frac{f_m\delta_{im}}{\omega_m}\sin\gamma_2 \tag{6.35}$$

$$a_m\beta_m' = -\frac{S_{mm}a_m^3}{\omega_m} - \frac{S_{mn}a_m a_n^2}{\omega_m} - \frac{\Lambda_m a_n a_m^2}{\omega_m}\cos\gamma_1 - \frac{f_m\delta_{im}}{\omega_m}\cos\gamma_2 \tag{6.36}$$

where γ_1 and γ_2 are defined as

$$\gamma_1 = \sigma_1 T_2 - 3\beta_m + \beta_n,\ \ \gamma_2 = \sigma_2 T_2 - \delta_{in}\beta_n - \delta_{im}\beta_m$$

Consequently, the microbeam dynamic response to second order can be expressed as

$$\begin{aligned} u(x,t) = {} & a_n\cos(\omega_n t + \beta_n)\phi_n(x) + a_m\cos(\omega_m t + \beta_m)\phi_m(x) \\ & + \frac{1}{2}a_n^2\left[\cos 2(\omega_n t + \beta_n)\psi_{in}(x) + \psi_{2n}(x)\right] \\ & + \frac{1}{2}a_m^2\left[\cos 2(\omega_m t + \beta_m)\psi_{im}(x) + \psi_{2m}(x)\right] \\ & + \frac{1}{2}a_n a_m[\cos((\omega_n + \omega_m)t + \beta_n + \beta_n)\psi_3(x) \\ & + \cos((\omega_n - \omega_m)t + \beta_n - \beta_m)\psi_4(x)] + \cdots \end{aligned} \tag{6.37}$$

where a_n, a_m, β_n, and β_m are governed by equations (6.33)-(6.36).

6.2.2 Results

We consider the case in which the first mode is directly excited with a primary resonance ($f_n = 0$) when $\omega_2 \approx 3\omega_1$. We solved the boundary-value problem, equations (3.9), for the static deflection. Then using this deflection, we solved equations (3.13) to determine the first and second natural frequencies and mode shapes. Using these results, we solved equations (6.27) and (6.28) for the ψ's and then evaluated the χ's. Finally, we calculated the S_{ij}, Λ_i, and f_m.

We considered three cases. The first case corresponds to $\alpha_1 = 3.70$, $\alpha_2 V_p^2 = 35.30$,

and $N = 0$; the first and the second natural frequencies are $\omega_1 = 20.35$ and $\omega_2 = 61$. The second case corresponds to $\alpha_1 = 3.70$, $\alpha_2 V_p^2 = 5.50$, and $N = -10$; the natural frequencies are $\omega_1 = 19.12$ and $\omega_2 = 57.70$. The last case corresponds to $\alpha_1 = 3.70$, $\alpha_2 V_p^2 = 56.80$, and $N = 10$, and the natural frequencies are $\omega_1 = 21.60$ and $\omega_2 = 64.20$. For all three cases, the numerical results show that the nonlinear interaction coefficients Λ_i vanish identically, which precludes the possibility of activating this internal resonance. Hence, although the ratio between the natural frequencies is close to three-to-one, the first and second modes do not exchange energy. This is expected because the first mode is symmetric, the second mode is antisymmetric, and the static deflection is symmetric.

Chapter 7

Dynamic Behavior of Microbeams under a DC Electrostatic Force

We derived in Chapter 3 a discretized system of equations to simulate the mechanical behavior of microbeams when actuated by a DC electrostatic force. In Chapter 4, we used a reduced-order model derived from the discretized system to simulate the static behavior of microbeams. We concluded that the proposed reduced-order model is very efficient and can predict successfully the static behavior even in cases of stiff boundary-value problems and near pull-in.

In this chapter, we use the reduced-order model to predict the dynamic behavior of electrostatically actuated microbeams. We compute the pull-in time, which is an important parameter in capacitive microswitches, and verify the capability of the reduced-order model to predict the dynamic behavior by comparing our results with available experimental results.

We consider a microbeam actuated by a DC electrostatic force. The time it takes a DC input signal to grow from a zero voltage to the steady-state voltage, also called rise time, is typically very short. We assume a typical value for the rise time equal to 8×10^{-10} s. We use symmetric modes in the discretization because the microbeam

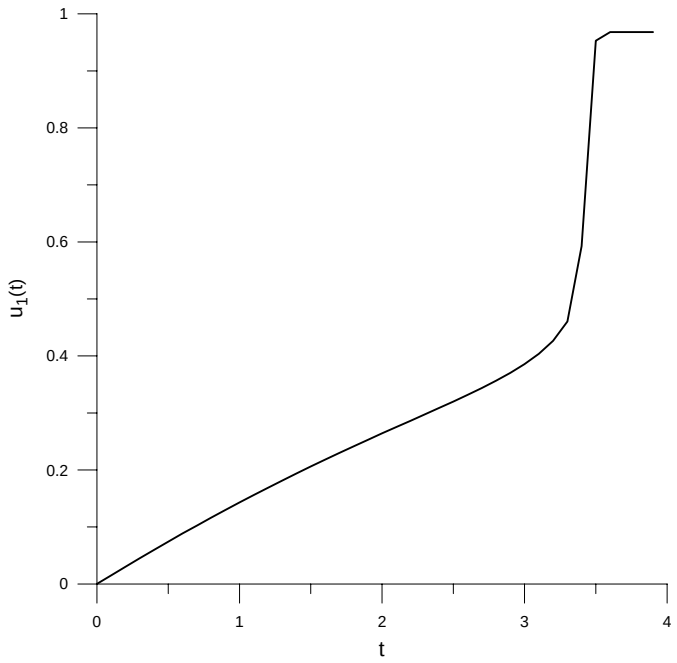

Figure 7.1: Evolution of u_1 with the nondimensional time showing the onset of pull-in. The results are obtained using a nondimensional damping coefficient c =260 and a DC voltage V_p=10 V.

shape remains symmetric during the motion. First, we solve the linear-undamped eigenvalue problem, equations (3.17), for the ϕ_i and ω_i. Then, we plug the results into equations (3.19) and integrate them in time for the $u_i(t)$. To obtain the deflection at any DC voltage V_p and at any time, we use equation (3.16) with the ϕ_i and $u_i(t)$. We find the pull-in time by integrating equations (3.19) in time until a sudden rise in the displacement occurs, at which we report the time as the pull-in time. We use the design specifications of Hung and Senturia [22] for a microbeam of $l = 610\mu m$, $h = 2.2\mu m$, $b = 40\mu m$, $d = 2.3\mu m$. The reported experimental pull-in voltage is V_p=8.76 V. Hung and Senturia [22] assumed the microbeam to be subject to an axial stress of -3.7 MPa so that their theoretical pull-in voltage matches the experimental value. Because h is given as a nominal value, we modify it to match the pull-in voltage. Accordingly, we let $h = 2.015\mu m$.

Figure 7.1 shows a plot of the evolution of u_1, which is the dominant coefficient, with the nondimensional time obtained by integrating equations (3.19) using the first

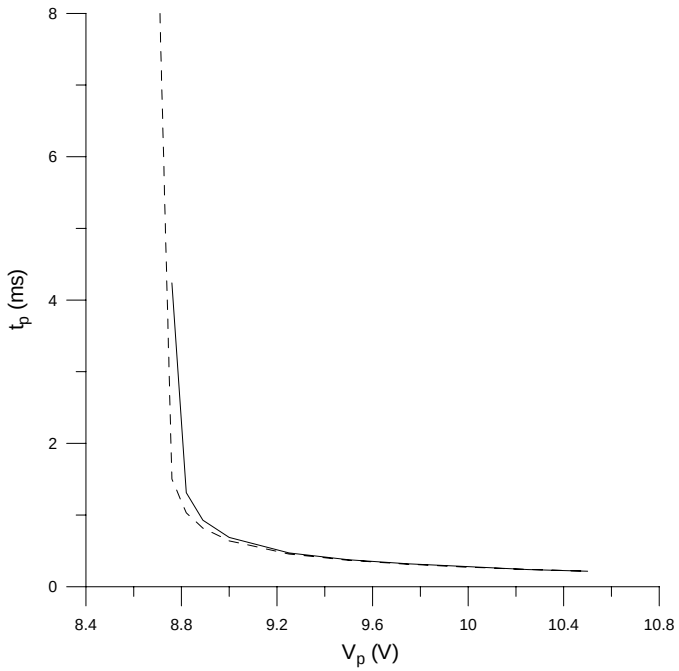

Figure 7.2: Comparison of the pull-in time obtained using the first three symmetric modes (dashed line) with that obtained using the first five symmetric modes (solid line) for various values of V_p and c =260.

five symmetric modes. We use a nondimensional damping coefficient c =260 and a DC voltage V_p=10 V. As can be seen in the figure, the nondimensional pull-in time is approximately located at t=3.4, where a sudden rise in u_1 occurs.

Figure 7.2 shows a comparison of the pull-in time t_p obtained using the first three symmetric modes (dashed line) with that obtained using the first five symmetric modes (solid line) for various values of V_p, which are beyond the pull-in voltage. We used the data of Hung and Senturia [22] in the calculations with a nondimensional damping coefficient c =260. We note that close to the pull-in voltage, the curve obtained with the three-mode approximation deviates significantly from that obtained with the five-mode approximation. However, both curves gradually move close to each other on increasing V_p away from the pull-in voltage.

In Figure 7.3, we compare the calculated pull-in time using our theory with the theoretical and experimental results of Hung and Senturia [22] for various values of V_p.

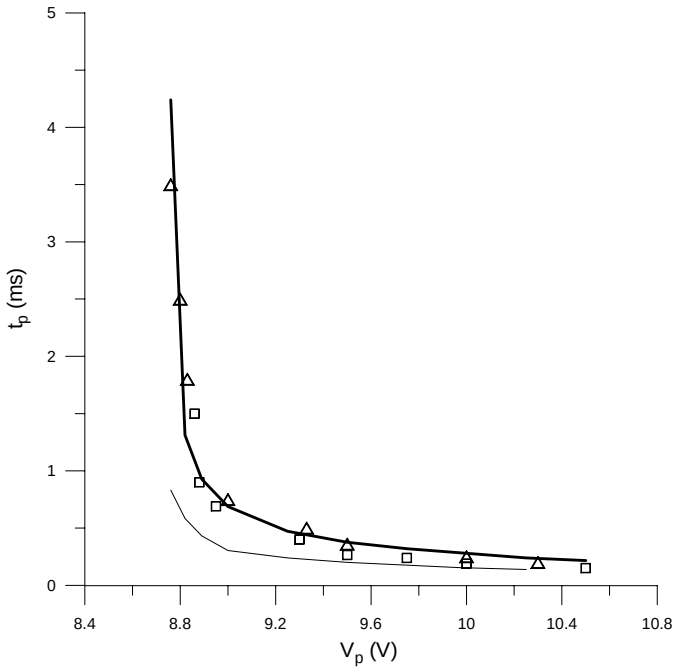

Figure 7.3: Comparison of the pull-in time t_p obtained using our model (solid lines) with those obtained theoretically (squares) and experimentally (triangles) by Hung and Senturia [22]. The thin solid line is based on the a nondimensional damping coefficient c =160 estimated by Gupta and Senturia [35] for the same device in [22] and the thick solid line is based on the nondimensional damping coefficient c =260 estimated using our model.

The discrete points, triangles and squares, are the experimental and theoretical results obtained by Hung and Senturia [22], respectively. The theory of Hung and Senturia [22] is based on using a reduced-order model generated by discretizing the original equations of motion using the Galerkin method. Hung and Senturia [22] generated their basis functions using data produced from a few runs of fully meshed and a slow finite-difference method. They solved two coupled partial-differential equations (PDE): the first describes the microbeam behavior under the electrostatic force in the presence of damping, and the second relates the damping to the pressure and the microbeam deflection. The thin solid line was obtained using the first five symmetric mode and the nondimensional damping coefficient c=160 estimated by Gupta and Senturia [35] for the same device in [22]. Gupta and Senturia [35] obtained the damping coefficient by matching the experimental pull-in time to the one they calculated using a single-degree-

of-freedom model. We note that our results are poor compared to the experimental results. We determined another coefficient by matching the pull-in time obtained using equations (3.19) at $V_p = 8.83\ V$ to the experimental value of Hung and Senturia [22]. The extracted coefficient is c=260 and the results obtained using this value are shown in Figure 7.3 as the thick solid line. We note that the results are in excellent agreement with the experimental results.

We conclude that using the first five symmetric modes in the proposed reduced-order model accurately simulate the mechanical behavior of electrostatically actuated microbeams.

Chapter 8

Concluding Remarks and Recommendations

8.1 Summary

8.1.1 Static Behavior and Natural Frequencies of Microbeams under a DC Electrostatic Force

We studied the static behavior and the free vibration of an electrostatically actuated microbeam using a model accounting for mid-plane stretching and the nonlinear electrostatic forcing. We presented results describing the static and dynamic characteristics of the microbeam and compared them to experimental results available in the literature. The agreement is excellent, which validates the proposed model.

We found two static solutions at each DC value by solving a nonlinear boundary-value problem and by solving a reduced-order discretized model. We studied the local stability of these solution by calculating the Jacobian matrix of the discretized system of equations associated with each solution and computed its eigenvalues. The results show that the larger solution is unstable with at leat one eigenvalue being positive. At pull-in, both solutions coalesce with an eigenvalue approaching zero. Beyond the pull-in voltage, both solutions disappear in a saddle-node bifurcation.

We found maximum nondimensional deflections of up to 0.45 near pull-in, signif-

icantly above the traditionally used stability limit of $W_{Max} \leq \frac{1}{3}$. This indicates the importance of including mid-plane stretching in the analysis to avoid underestimation of the stability limits.

Increasing the axial force N was found to increase the level of electrostatic forcing at pull-in, but, characteristically, the nonlinear behavior of the resonator is unaffected. On the other hand, increasing the mid-plane stretching represented by α_1 was found to increase the level of electrostatic forcing at pull-in *and* to change the nonlinear behavior of the resonator. So, whereas α_1 or N can be used by designers to create a wider operation range, *only* α_1 can be tuned to yield a linear relationship between the natural frequency and voltage. This is a very significant result. In conjunction with the model's ability to predict the microbeam behavior for any DC polarization voltage, it allows designers to use a much wider range of DC polarization voltages.

Sometimes in the literature an applied axial force is added to a microbeam model to compensate for the neglected mid-plane stretching by matching the theoretical and experimental pull-in voltages. The present theory shows that, although the pull-in voltage can be increased either by increasing α_1 or N, they are not equivalent and each leads to a totally different behavior. Thus, compensating for mid-plane stretching by an axial force might produce errors.

8.1.2 Nonlinear Response of Microbeams to an Electric Actuation

We studied the nonlinear dynamic response of a microbeam that is actuated by a general electric load, subject to an applied axial load, and accounting for mid-plane stretching. We used the method of multiple scales to determine the response to a primary resonance excitation of the first mode and obtained two nonlinear first-order ordinary-differential equations governing the amplitude and phase of the response. We derived an equation that describes the nonlinear resonance frequency of the microbeam as a function of the damping and the effective nonlinearity coefficient. This equation shows that increasing the AC forcing and/or decreasing the damping leads to either an increase or a decrease in the nonlinear resonance frequency, depending on the sign of the effective nonlinearity coefficient. We compared the nonlinear resonance frequency

computed using our theory to the experimental results available in the literature. We found excellent agreement.

We studied the effect of the nondimensional design parameters N, α_1, and $\alpha_2 V_p^2$ on the normalized nonlinear resonance frequency $\frac{\Omega_r}{\omega}$. The results show that increasing N, the axial force, improves the linear characteristics of $\frac{\Omega_r}{\omega}$ and decreases the frequency shift. In contrast, increasing α_1, the mid-plane stretching, has the reverse effect on $\frac{\Omega_r}{\omega}$. The nonlinear analysis reveals that the two parameters directly influence the mid-plane stretching of the microbeam. On the other hand, $\alpha_2 V_p^2$ affects the qualitative and quantitative nature of the effective nonlinearity coefficients of the system. The sign of S changes from positive, corresponding to a hardening behavior, to negative corresponding to a softening behavior. This is because the electric quadratic nonlinearity drastically decreases and overcomes the influence of the geometric nonlinearity. We note that most of the models used in the literature neglect the effect of the quadratic nonlinearity. Instead, they assume the nonlinearity of the system to be solely cubic, which predicts a harding behavior rather than the correct softening behavior. Therefore failure to correctly account for the nonlinearities in the system may lead to erroneous results. It is interesting to note that, for the studied case, this reverse in behavior occurs at a value of $\alpha_2 V_p^2$ that is about 65% of the pull-in limit. Because at this value the coefficient S is equal to zero, the dynamic response is theoretically linear. However, the simulation results show that $\frac{\Omega_r}{\omega}$ becomes highly sensitive to any slight changes in $\alpha_2 V_p^2$. This indicates that, although it is possible to compensate for the effect of the electrostatic force with the mid-plane stretching, operations near such conditions are unstable and impractical.

We applied the method of multiple scales to investigate possibility of a three-to-one internal resonance between the first and second modes, which if exists can adversely affect the performance of the resonator. The analysis shows that these two modes are nonlinearly uncoupled, and hence this internal resonance cannot be activated. This result enhances the reliability of such a device.

In conclusion, the present nonlinear model provides an accurate prediction of the dynamic behavior of microbeams, which linear models fail to explain. Unlike existing

models in the literature, the present nonlinear model is capable of simulating the mechanical behavior of microbeams for general operating conditions and for a wide range of applied electric loads. Further, by using the perturbation solution, one can easily derive analytical expressions that present a clearer picture of the influence of various design parameters, which is critical for improving and optimizing designs.

8.1.3 Reduced-Order Models of Microbeams

To simulate the behavior of microbeams under a DC electrostatic force, we developed a new technique to treat the electrostatic force when discretizing the equation of motion. The new method allows the use of few linear-undamped mode shapes of a straight beam as basis functions in a Galerkin procedure, and hence reduces the complexity of the simulation and reduces significantly the computational time.

We discussed two approaches for treating the electrostatic force term in the discretized system of equations. In the first, we expand $\frac{1}{(1-w)^2}$ in a Taylor series around w=0 up to fifth order. We showed that this method fails to represent correctly the electrostatic force because the expansion diverges as w approaches unity. Then, we introduced a new method in which we multiply the equation of motion by $(1-w)^2$, and hence represent the electrostatic force in the discretized equations without approximation. We validated the proposed reduced-order model by simulating the static behavior of the microbeam and comparing the results with available experimental results. We found excellent agreement. Then, we validated the reduced-order model by computing the pull-in times and comparing them with experimental results in the literature. We also found good agreement.

In conclusion, the proposed reduced-order model, which uses the linear-undamped mode shapes of undeflected microbeams, is capable of predicting the static and dynamic behavior of electrostatic MEMS. The use of linear mode shapes, which are easy to calculate, in the discretization is very attractive compared with running huge finite-element method packages to extract the basis functions. Finite-element methods are generally expensive, complex, slow, and inconvenient for understanding the effects of various design parameters.

The present reduced-order model possesses attractive features over the other models. It predicts the static behavior and the pull-in voltage accurately by solving an algebraic system of equations, which is computationally easier to implement compared to other complicated numerical techniques. Numerical methods for solving the boundary-value problem usually suffer from the stiffness of the equations and may become unstable, especially as the pull-in voltage is approached. We demonstrated that the reduced-order model can handle very stiff problems and accurately predict the pull-in voltage.

Another important advantage for using a reduced-order model of discretized system of equations is the ability to study the local and global dynamics and their stability. Thus, one is able to investigate many possible nonlinear phenomena, which may not be predicted by attacking directly the boundary-value problem or by using finite-element methods.

8.2 Recommendations for Future Work

The research in the electrostatic MEMS area is still in its preliminary stage. There are many topics and unclear points that need to be investigated to ensure the reliability of these devices before entering the market. In what follows, we list recommendations and notes for future work :

- Experimental work needs to be conducted to better understand the behavior of resonant microbeams near the critical value of DC voltage at which the behavior is reversed from softening to hardening.
- An investigation of other possible internal resonances in resonant microbeams, such as a two-to-one internal resonance between the second and third modes.
- A global investigation of the behavior of microbeams in resonant sensors needs to be conducted using a reduced-order model.
- An investigation needs to be conducted into the effect of temperature variations on resonant sensors.

- In the developed reduced-order model, an even number of symmetric modes fails to predict the correct behavior, while using an odd number does not have such a problem. Therefore, this strange behavior needs to be investigated.

- The present model is based on symmetric uniform beams. We recommend development of models for asymmetric beams and other mechanical elements, such as circular diaphragms and narrow beams with a rectangular paddle.

- A feasibility study of using the deflected mode shapes in the discretization procedure needs to be carried out and comparing the results with those obtained using the undeflected mode shapes to check whether the number of modes can be reduced.

- An investigation needs to be carried out into the neglected effects in modeling the behavior of microbeams in capacitive microswitches. These include the fringes of the electrostatic field, nonlinear damping, and loss of energy due to the contact of the microbeam with the substrate, which is important for calculating the pull-out time (the time a microbeam in the on-state takes to respond to a zero voltage to return to the off-state).

Appendix A : Rayleigh's Energy Method

In this section, we use Rayleigh's energy method [36] to approximate the fundamental natural frequency of a straight microbeam of fixed-fixed ends. Tilmans et al. [4] has studied the same problem, but they misrepresented the mid-plane stretching in their derivation. We compare our equation with that of Tilmans et al. [4] and show the mistake. We then discuss the theory of Tilmans and Legtenberg [7], which is based on [4], in deriving an equation that governs the nonlinear resonance frequency of a microbeam under electric forces. We compare their equation with equation (6.22), which we have obtained from a perturbation analysis using the method of multiple scales.

We consider the microbeam shown in Figure 3.1 with zero AC and DC forces. To obtain the equation that governs the microbeam motion, we set V_p and $v(t)$ equal to zero in equation (3.3), assume the same boundary conditions as in equation (3.4), and obtain

$$\frac{EI}{1-\nu^2}\frac{\partial^4 w}{\partial x^4}+\rho bh\frac{\partial^2 w}{\partial t^2}+\hat{c}\frac{\partial w}{\partial t}=\left[\frac{EA}{2\ell(1-\nu^2)}\int_0^\ell\left(\frac{\partial w}{\partial x}\right)^2 dx+\hat{N}\right]\frac{\partial^2 w}{\partial x^2} \tag{A.1a}$$

$$w(0,t)=w(\ell,t)=0, \qquad \frac{\partial w(0,t)}{\partial x}=\frac{\partial w(\ell,t)}{\partial x}=0 \tag{A.1b}$$

To derive an expression for the Rayleigh quotient of the undamped system ($\hat{c}=0$) of equations (A.1), we first derive the system energy. We multiply equation (A.1a) by $\frac{\partial w}{\partial t}$, integrate the result by parts from $x=0$ to $x=\ell$, and use equation (A.1b). Then,

by realizing that the result is the rate of change of the system's total energy H, we obtain the following energy equations:

$$H = U + T \tag{A.2a}$$

$$U = \frac{EI}{2(1-\nu^2)} \int_0^\ell \left(\frac{\partial^2 w}{\partial x^2}\right)^2 dx + \frac{1}{2}\hat{N} \int_0^\ell \left(\frac{\partial w}{\partial x}\right)^2 dx + \frac{EA}{8\ell(1-\nu^2)} \left[\int_0^\ell \left(\frac{\partial w}{\partial x}\right)^2 dx\right]^2 \tag{A.2b}$$

$$T = \frac{1}{2}\rho bh \int_0^\ell \left(\frac{\partial w}{\partial t}\right)^2 dx \tag{A.2c}$$

where U and T are the potential and kinetic energies of the system, respectively.

The generic form of Rayleigh quotient can be defined [36] as

$$\omega^2 = \frac{U_{max}}{T_{ref}} \tag{A.3}$$

where ω is the approximate fundamental natural frequency, U_{max} is the maximum potential energy whereby the time dependence is eliminated, and T_{ref} is the reference kinetic energy, which is defined below in equation (A.5b). To this end, we separate the variables by assuming a harmonic motion of the microbeam as

$$w(x,t) = \phi(x)\cos(\omega t) \tag{A.4}$$

where $\phi(x)$ is an admissible function that satisfies at least the geometric boundary conditions of equation (A.1b). Substituting equation (A.4) into equations (A.2b) and (A.2c), we obtain

$$U = \left\{ \frac{EI}{2(1-\nu^2)} \int_0^\ell \left(\frac{\partial^2 \phi}{\partial x^2}\right)^2 dx + \frac{1}{2}\hat{N} \int_0^\ell \left(\frac{\partial \phi}{\partial x}\right)^2 dx + \frac{EA\cos^2(\omega t)}{8\ell(1-\nu^2)} \left[\int_0^\ell \left(\frac{\partial \phi}{\partial x}\right)^2 dx\right]^2 \right\} \cos^2(\omega t) \tag{A.5a}$$

$$T = \omega^2 \frac{1}{2}\rho bh \sin^2(\omega t) \int_0^\ell \phi^2 dx = \omega^2 T_{ref} \sin^2(\omega t) \tag{A.5b}$$

By setting $\cos(\omega t) = \pm 1$ in equation (A.5a), we obtain U_{max}. Substituting U_{max}

and T_{ref}, shown in equation (A.5b), into equation (A.3), we obtain the Rayleigh quotient

$$\omega^2 = \frac{\frac{EI}{2(1-\nu^2)}\int_0^\ell \left(\frac{\partial^2\phi}{\partial x^2}\right)^2 dx + \frac{1}{2}\hat{N}\int_0^\ell \left(\frac{\partial\phi}{\partial x}\right)^2 dx + \frac{EA}{8\ell(1-\nu^2)}\left[\int_0^\ell \left(\frac{\partial\phi}{\partial x}\right)^2 dx\right]^2}{\frac{1}{2}\rho bh\int_0^\ell \phi^2 dx} \tag{A.6}$$

Equation (A.6) gives an upper estimate for the fundamental natural frequency of an unactuated fixed-fixed microbeam, which can be equal to the exact value if the first mode shape is used as the admissible trial function.

Tilmans et al. [4] studied the same problem, but they misrepresented the potential energy due to mid-plane stretching by expressing it as

$$U_{mid} = \frac{EA}{8}\int_0^\ell \left(\frac{\partial w}{\partial x}\right)^4 dx$$

The correct representation however is the last term in equation (A.2b), which also agrees with the result reported by Mehner et al. [24].

Next, we reproduce the theory of Tilmans and Legtenberg [7] to derive an equation for the nonlinear resonance frequency of a resonator under electric forces. Tilmans and Legtenberg [7] used a single-degree-of-freedom system to relate the maximum amplitude of vibration w_{max} to the electric forces as

$$w_{max} = \frac{Qd\psi V_{AC}}{V_{PI}} \tag{A.7}$$

where $\psi = 0.25c_1^2\frac{V_p}{V_{PI0}}$, c_1 is a constant depends on the choice of the admissible function and V_{PI0} is the pull-in voltage of uniform electrodes [7]. The other parameters are defined in Section 3.1. The maximum amplitude of vibration w_{max} is related to the maximum amplitude of the admissible trial function ϕ_{max} as

$$w_{max} = \phi_{max}\cos(\omega t) \tag{A.8}$$

Based on (A.8), Tilmans and Legtenberg [7] substituted for $\cos(\omega t) = \frac{w_{max}}{\phi_{max}}$ in the coefficient of mid-plane stretching in equation (A.5a), and substituted $\cos^2(\omega t) = 1$

and $\sin^2(\omega t) = 1$ to obtain U_{max} and T_{ref}. The result is then substituted into equation (A.3) and w_{max} is replaced using equation (A.7). After some manipulation, they obtained the following equation that approximates the nonlinear resonance frequency of the resonator:

$$\Omega_r = \omega_1 \left[1 + \frac{\hat{\beta}(\frac{d}{h})^2 V_p^2 V_{AC}^2 Q^2}{K(1 + \hat{\gamma}\frac{\hat{N}}{Ebh}(\frac{\ell}{h})^2)} \right]^{\frac{1}{2}} \tag{A.8}$$

where K is a constant that depends on the choice of the admissible function and on the pull-in voltage of the system and ω_1, $\hat{\beta}$, and $\hat{\gamma}$ are as follows [4]:

$$\omega_1^2 = \frac{\alpha_1^4 EI}{\ell^4 \rho A(1-\nu^2)} \left(1 + \hat{\gamma}\frac{N\ell^2)}{12EI} \right) \tag{A.9}$$

$$\alpha_1^2 = \ell^2 \left[\frac{\int_0^\ell \left(\frac{\partial^2 \phi}{\partial x^2}\right)^2 dx}{\int_0^\ell \ \phi^2 dx} \right]^{\frac{1}{2}} \tag{A.10}$$

$$\hat{\gamma} = \frac{12(1-\nu^2)\int_0^\ell \left(\frac{\partial \phi}{\partial x}\right)^2 dx}{\ell^2 \int_0^\ell \left(\frac{\partial^2 \phi}{\partial x^2}\right)^2 dx} \tag{A.11}$$

$$\hat{\beta} = \frac{3\int_0^\ell \left(\frac{\partial \phi}{\partial x}\right)^4 dx}{\phi_{max}^2 \int_0^\ell \left(\frac{\partial^2 \phi}{\partial x^2}\right)^2 dx} \tag{A.12}$$

The parameter ω_1 is the approximate fundamental natural frequency of a straight microbeam excluding mid-plane stretching.

The coefficient of mid-plane stretching β is corrected according to our derivation

as

$$\hat{\beta} = \frac{3(1-\nu^2)\left(\int_0^\ell \left(\frac{\partial \phi}{\partial x}\right)^2 dx\right)^2}{\ell \phi_{max}^2 \int_0^\ell \left(\frac{\partial^2 \phi}{\partial x^2}\right)^2 dx} \tag{A.13}$$

Expanding equation (A.8) around one up to first order, we obtain

$$\Omega_r = \omega_1 \left[1 + \frac{\hat{\beta}(\frac{d}{h})^2 V_p^2 V_{AC}^2 Q^2}{2K(1+\hat{\gamma}\frac{\hat{N}}{Ebh}(\frac{\ell}{h})^2)}\right] + {}_{3}.. \tag{A.14}$$

By comparing equation (A.14) with equation (6.22), we note that, in both equations, the nonlinear resonance frequency Ω_r has the same dependence on Q and V_{AC}. Equation (A.14) accounts for the geometric cubic nonlinearity of the system via the coefficient β but neglects the other nonlinearities of the system. Equation (6.22), on the other hand, represents completely the geometric and electric nonlinearities of the system as well as their types whether quadratic or cubic. Thus, equation (6.22) gives a more general and accurate prediction for Ω_r, which may increase or decrease depending on how the various nonlinearities affect the magnitude and the sign of the effective nonlinearity coefficient S. An example of a such variation is shown in Figure 6.8. Moreover, the accuracy of the results of Rayleigh's energy method depend on how close the choice of the admissible function is to the exact mode shape, which depends on the DC force.In contrast, equation (6.22) does not suffer from such a problem because it uses directly the exact mode shapes, which are obtained numerically prior to using equation (6.22).

References

1. Ehmke, J., Brank, J., Malczewski, A., Pillans, B., Eshelman, S., Yao, J., and Goldsmith, C., "RF MEMS devices: a brave new world for RF technology, " Ratheon Systems Company, P.O.box 660240, Dallas, TX 75266.

2. Younis, M. I., Abdel-Rahman, E. M., and Nayfeh, A. H., "Static and dynamic behavior of an electrically excited resonant microbeam," accepted to the AIAA 43rd Structures, Structural Dynamics, and Materials Conference, Denver, CO, April 2002.

3. Nayfeh, A. H., *Nonlinear Interactions,* Wiley, New York, 2000.

4. Tilmans, H. A., Elwespoek, M., and Fluitman, J. H., "Micro resonant force gauges," Sensors and Actuators A, Vol. 30, 1992, pp. 35–53.

5. Zook, J. D., Burns, D. W., Guckel, H., Sniegowski, J. J., Engelstad, R. L., and Feng, Z., "Characteristics of polysilicon resonant microbeams," Sensors and Actuators A, Vol. 35, 1992, pp. 290–294.

6. Ijntema, D. J. and Tilmans, H. A., "Static and dynamic aspects of an air-gap capacitor," Sensors and Actuators A, Vol. 35, 1992, pp. 121–128.

7. Tilmans, H. A. and Legtenberg, R., "Electrostatically driven vacuum-encapsulated polysilicon resonators. Part II. Theory and performance," Sensors and Actuators A, Vol. 45, 1994, pp. 67–84.

8. Choi, B. and Lovell, E. G., "Improved analysis of microbeams under mechanical and electrostatic loads," Journal of Micromechanics and Microengineering, Vol.

7, 1997, pp. 24–29.

9. Ahn, Y., Guckel, H., and Zook, J. D., "Capacitive microbeam resonator design," Journal of Micromechanics and Microengineering, Vol. 11, 2001, pp. 70–80.

10. Gui, C., Legrenberg, H., Tilmans, A. C., Fluitman, J. H. J., and Elwenspoek, M.,"Nonlinearity and hysteresis of resonant strain gauges," Journal of Microelectromechanical Systems, Vol. 7, 1998, pp. 122–127.

11. Turner, G. C. and Andrews, M. K., "Frequency stabilization of electrostatic oscillators," in The 8th International Conference on Solid-State Sensors and Actuators, Sweden, 1995, pp. 25–29.

12. Ayela, F. and Fournier, T., "An experimental study of anharmonic micromachined silicon resonators," Measurement, Science and Technology, Vol. 9, 1998, pp. 1821–1830.

13. Veijola, T., Mattila, T., Jaakkola, O., Kiihamaki, J., Lamminmaki, T., Oja, A., Ruokonen K., Seppala, H., and Tittonen, I., "Large-displacement modeling and simulation of micromechanical electrostatically driven resonators using the harmonic balance method," Microwave Symposium Digest. 2000 IEEE MTT-S International, Vol. 1, 2000, pp. 11–16.

14. Zavracky, P. M., Majumder, S., and McGruer, N. E., "Micromechanical switches fabricated using nickel surface micromachining," Journal of Microelectromechanical Systems, Vol. 6, 1997, pp. 3–9.

15. Chan, E. K., Garikipati, K., and Dutton, W. R., " Characteristics of contact electromechancs through capacitance-voltage measurements and simulations," Journal of Microelectromechanical Systems, Vol. 8, 1999, pp. 208–217.

16. Grtétillat, M. A., Grtétillat, F., and Rooij, N. F., "Micromechanical relay with electrostatic actuation and metallic contacts," Journal of Micromechanics and Microengineering, Vol. 9, 1999, pp. 324–331.

17. Yao, Z. J., Chen, S., Eshelman, S., Denniston, D., and Goldsmith, C., "Micromachined low-loss microwave switches," Journal of Microelectromechanical Systems, Vol. 8, 1999, pp. 129–134.

18. Senturia, S. D., Harris, R. M., Johnson, B. P., Kim, S., Nabors, K., Shulman, M. A., and White, J. K., "A computer-aided design system for microelectromechanical systems (MEMCAD)," Journal of Microelectromechanical Systems, Vol. 1, 1992, pp. 3–13.

19. Gillbert, J. R., Legtenberg, R., and Senturia, S. D., "3D coupled electro-mechanics for MEMS: applications of CoSolve-EM," in Proceedings of the IEEE Micro Electro Mechanical Systems, MEMS '95, 1995, pp. 122–127.

20. Grtétillat, M. A., Yang, Y. J., Hung, E. S., Rabinovich, V., Ananthasuesh, G. K., Rooij, N. F., and Senturia, S. D., "Nonlinear electromechanical behavior of an electrostatic microrelay," in Iternational Conference on Solid State Sensors and Actuators, TRANSDUCERS '97, Chicago., IL, Vol. 2, 1997, pp. 1141–1144.

21. Castañer, L. M. and Senturia, S. D., "Speed-energy optimization of electrostatic actuators based on pull-in," Journal of Microelectromechanical Systems, Vol. 8, 1999, pp. 290–298.

22. Hung, E. S. and Senturia, S. D., "Generating efficient dynamical models for microelectromechanical systems from a few finite-element simulations runs," Journal of Microelectromechanical Systems, Vol. 8, 1999, pp. 280–289.

23. Gabbay, L. D., Mehner, J. E., and Senturia, S. D., "Computer-aided generation of nonlinear reduced-order dynamic macromodels I: Non-stress-stiffened case," Journal of Microelectromechanical Systems, Vol. 9, 2000, pp. 262–269.

24. Mehner, J. E., Gabbay, L. D., and Senturia, S. D., "Computer-aided generation of nonlinear reduced-order dynamic macromodels II: Stress-stiffened case," Journal of Microelectromechanical Systems, Vol. 9, 2000, pp. 270–278.

25. Fan, S., Liu, G., and Lee, M. H., "Finite-element modeling and simulation on frequency characteristics of the silicon beam resonator attached to an E-type round diaphragm for measuring the concentrated force," Sensors and Actuators A, Vol. 63, 1997, pp. 169–176.

26. Jin, Z. and Wang, Y., "Electrostatic resonator with second superharmonic resonance," Sensors and Actuators A, Vol. 64, 1998, pp. 273–279.

27. Tilmans, H. A. and Legtenberg, R., "Electrostatically driven vacuum-encapsulated polysilicon resonators. Part I. Design and fabrication," Sensors and Actuators A, Vol. 45, 1994, pp. 57–66.

28. Huang, J. M., Liew, K. M., Wong, C. H., Rajendran, S., Tan, M. J., and Liu, A. Q., "Mechanical design and optimization of capacitive micromachined switch," Sensors and Actuators A, Vol. 93, 2001, pp. 273–285.

29. Musalem, F. X., "MEMS-based RF switches," Mechanical Engineering, Mechanical Engineering Design, Vol. 123, 2001, pp. 22–25.

30. Griffiths. D. J., *Introduction to Electrodynamics,* Prentice Hall, New Jersey, 1981.

31. Nayfeh, A. H. and Mook, D. T., *Nonlinear Oscillations,* Wiley, New York, 1979.

32. Seeger, J. I. and Crary, S. B., "Stabilization of electrostatically actuated mechanical devices," TRANSDUCERS'97: International Conference on Solid-State Sensors and Actuators, Chicago, IL, 1997, pp. 1133–1136.

33. Nayfeh, A. H., *Introduction to Perturbation Techniques,* Wiley, New York, 1981.

34. Nayfeh, A. H. and Balachandran B., *Applied Nonlinear Dynamics,* Wiley, New York, 1995.

35. Gupta, R. K. and Senturia, S. D., "Pull-in time dynamics as a measure of absolute pressure," in Proceedings of the IEEE Micro Electro Mechanical Systems, MEMS '97, 1997, pp. 290–294.

36. Meirovitch, L., *Fundamentals of Vibrations,* McGraw-Hill, Boston, 2001.

Vita

Mohammad Ibrahim Younis was born on September 6, 1977 in Beredah City in Saudi Arabia. He Joined the Mechanical Engineering Department at Jordan University of Science and Technology, Irbid, Jordan, in 1994. He received his Bachelor of Science in June 1999. Then he worked at a private company as a consultant engineer in the field of pumps, pipes, and water sector until mid December 1999, where he joined the Department of Mechanical Engineering at King Fahad University of Petroleum and Minerals (KFUPM), Dhahran, Saudi Arabia, to study towards a Master degree. In October 2000, he transferred to the Department of Engineering Science and Mechanics at Virginia Polytechnic Institute and State University, Blacksburg, Virginia. On December 13, 2001, he successfully defended his Master thesis.